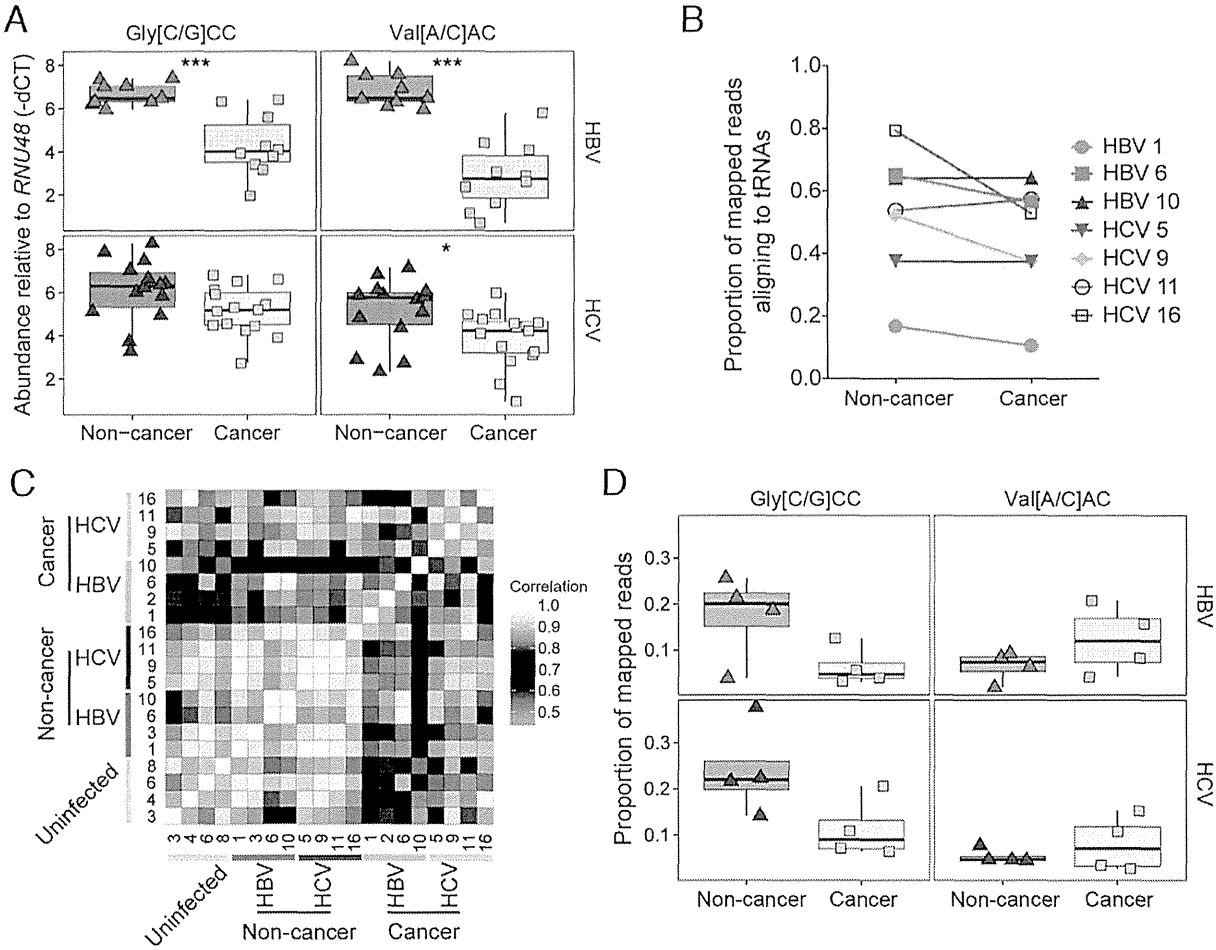

Figure 2 | 5′ tRH abundance in HBV- and HCV-associated hepatocellular carcinoma. (b) Abundance (RT-qPCR) of (left) 5′ tRH^{Gly} (Gly[C/G]CC) and (right) 5′ tRH^{Val} (Val[A/C]AC) in (top) non-malignant (n=9) and cancer tissue (n=10) from HBV-infected subjects, and (bottom) non-malignant (n=14), and cancer tissue (n=15) from HCV-infected subjects. Box and whisker plots are overlaid with data from each sample; whiskers extend to 1.5 * interquartile range. P-values calculated using Mann-Whitney U-test. *$P < 0.05$; **$P < 0.01$; ***$P < 0.005$. (b) Proportion of mapped reads aligning to tRNAs for the paired cancer and non-cancer tissue from subjects with chronic hepatitis B (n=3) and hepatitis C (n=4) (c) Correlation heatmap of tRNA-derived RNA expression profiles determined by small RNA sequencing. The colors of the cells represent Spearman's rank correlation coefficients of the relative levels of the 10 most abundant tRNA-derived RNAs between all pairs of tissue samples sequenced (n=20). (d) Proportion of mapped reads that align to 5′ tRH^{Gly} and 5′ tRH^{Val} in non-malignant and cancer tissue from (top) HBV-infected and (bottom) HCV-infected subjects. "Mapped reads" represents all reads aligning to miRNAs or tRNAs (see Methods).

abundance in seminal exosomes (considered to be immunosuppressive)[28], and roles in facilitating *Trypanosoma cruzi* infection in human cells and altering host gene expression[29].

There is good evidence that the abundance of these small non-coding RNAs increases in response to specific kinds of cellular stress. For example, tRHs are induced in cell culture by the addition of sodium arsenite, exposure to UV, nutrient starvation, hypoxia, hypothermia and heat, but not by exposure to etoposide, γ-radiation, caffeine[30,31]. This strongly suggests that the formation of tRHs is a regulated process, rather than due to general degradation of tRNAs in response to stress. In the nucleus angiogenin is involved in promoting angiogenesis[32] and in the cytoplasm, when not bound to RNH1, it acts as a tRNA-processing RNase[33,34], cleaving tRNAs at the anticodon loop and producing tRHs[30,31]. The cellular localization of angiogenin and its ribonuclease activity depend on the intracellular conditions and are regulated by RNH1[33]. The differences we observed in correlations between ANG expression and tRH abundance in chronic hepatitis B, hepatitis C and associated liver cancer may be a result of differences in angiogenin localization and function in these disease states. Non-tumor and tumor tissues from patients with chronic hepatitis C tend to show more evidence of angiogenesis than the in chronic hepatitis B[35,36]. This could mean that in chronic hepatitis C angiogenin is primarily nuclear, and therefore not exclusively involved in tRH production. Finally, it must also be noted that factors other than ANG may be critical to tRH biogenesis in different cell types or in response to different types of cellular stress. Much more remains to be uncovered about the specific mechanisms that lead to tRH accumulation.

Chronic infections with HBV and HCV typically lead to more severe liver disease in human patients than in the chimpanzee model[37,38]. Disease severity may account for the differences we observed in tRH abundance between liver tissue from human subjects with chronic HCV infection and the chimpanzee samples. Interestingly, however, humans and chimpanzees exhibited similar increases in tRH abundance in chronic hepatitis B, suggesting that

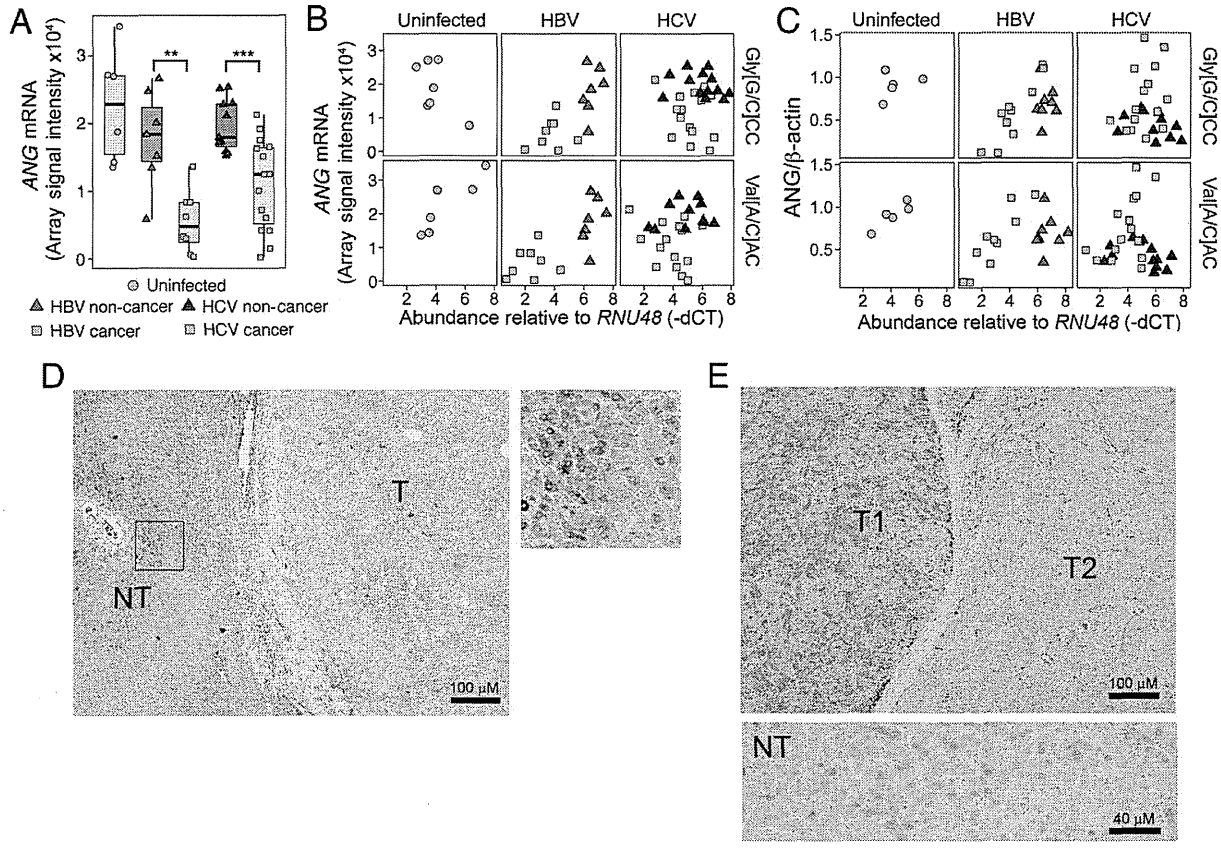

Figure 3 | Angiogenin expression in viral hepatitis and hepatocellular carcinoma. (a) Normalized *ANG* mRNA levels from previously generated liver microarray data[14] from uninfected subjects (n=6), non-malignant (n=7) and liver cancer (n=8) tissue from HBV-infected subjects, and non-malignant (n=11) and cancer tissue (n=15) from HCV-infected subjects. **P < 0.01; ***P < 0.005, calculated by Mann-Whitney *U*-test. (b) Scatter plot of the levels of 5′ tRHs (RT-qPCR, -dCT normalized to *RNU48*) and *ANG* mRNA (microarray). 5′ tRH^{Gly} ("Gly[C/G]CC"): uninfected subjects (n=7), non-cancer (n=7) and cancer (n=8) liver tissue from chronic hepatitis B subjects, and non-cancer (n=11) and cancer (n=15) liver tissue from chronic hepatitis C subjects; 5′ tRH^{Val}: uninfected subjects (n=6), non-cancer (n=7) and cancer (n=8) liver tissue from chronic hepatitis B subjects, and non-cancer (n=11) and cancer (n=15) liver tissue of chronic hepatitis C subjects. (c) Scatter plot of the levels of 5′ tRHs (RT-qPCR, -dCT normalized to *RNU48*) and ANG protein expression (normalized to β-actin) determined by immunoblot analysis. (d) Immunohistochemistry staining for ANG in formalin-fixed non-tumor (NT) and tumor tissue (T) from HBV-infected subject #10. (Right) Magnified view of non-tumor (NT). (e) ANG staining in adjacent tumor nodules (T1 and T2) and in non-tumor (NT) tissue from HCV-infected subject #7.

there may be a primary HBV-specific mechanism that directly regulates tRH biogenesis.

Our study has some technical limitations. tRNAs are subject to many different chemical modifications[39], several of which could impede library preparation and sequencing. This may have biased which tRNA-derived RNAs we detected. Also, we do not know how tRH abundance varies among the diverse cell types that populate the liver. Given that these small RNAs have not previously been studied in human tissue, we also have little appreciation of what functions these small non-coding RNAs have within the liver. Nonetheless, our finding that the intrahepatic abundance of tRHs is substantially increased in chronic viral infections of the liver and altered in HCC suggest that tRHs may have important, yet to be determined roles in liver disease. Thus, this study may have implications for disease pathogenesis and novel therapeutic strategies.

Methods

The methods were carried out in accordance with the approved guidelines.

Human subjects. Written informed consent was obtained from all human subjects. Ethics approval was obtained from the Ethics Committee for Human Genome/Gene Analysis Research at Kanazawa University Graduate School of Medical Science.

Chimpanzee liver tissue. The chimpanzee samples used in this study were archived from previous studies and were collected prior to December 15, 2011. Chimpanzees were housed and cared for at the Southwest National Primate Research Center (SNPRC) of the Texas Biomedical Research Institute. The animals were cared for in accordance with the Guide for the Care and Use of Laboratory Animals, and all protocols were approved by the Institutional Animal Care and Use Committee. SNPRC is accredited by the Association for Assessment and Accreditation of Laboratory Animal Care (AAALAC) International. SNPRC operates in accordance with the NIH and U.S. Department of Agriculture guidelines and the Animal Welfare Act. Animals were sedated for all procedures. Animals are group-housed with indoor and outdoor access and an environmental enrichment program is provided by a staff of behavioral scientists.

Small RNA-sequencing. RNA was isolated as described previously[14]. RNA purity was assessed with Nanodrop 2000 (Thermo Scientific) and integrity was determined with an Agilent 2100 Bioanalyzer (Agilent). RNA integrity and sequencing quality were comparable for all specimens (Supplemental Table 2–4). Small RNA libraries were generated using Illumina TruSeq Small RNA Sample Preparation Kit (Illumina, San Diego, CA). Sequencing was performed on Illumina HiSeq 2000 platform. Bioinformatic analysis: Sequencing reads were trimmed using Cutadapt (parameters O -10 e 0.1) and were further analyzed in two different ways: (i) Mapped trimmed reads allowing no mismatches to all tRNA sequences (except pseudo-tRNAs and undefined tRNAs) downloaded from GtRNAdb[16] (Figure 1b,c; Figure 2c,d; Supplemental Figure 1,2,4,7); (ii) Mapped trimmed reads to genomic regions spanning annotated miRNA s[40] (+/− 20 nts) and tRNA sequences (+/− 40 nts) using Bowtie 0.12.7[41] allowing for no mismatches. Next, reads that did not map

without mismatches were aligned to the same regions using SHRiMP2.2.2[42]. SHRiMP2.2.2 seeds were set based on the length of the read allowing 1 mismatch anywhere in the body and up to 3 mismatches at the 3′ end of the read (based on the length of the read). (Figure 1a right, Figure 2b, Supplemental Figure 7, Supplemental Table 4). Small RNA-sequencing data was deposited on GEO (GSE57381).

AGO2-RNA Co-immunoprecipitation. FT3-7 cells were grown in Dulbecco's modified Eagle's medium (DMEM, Life Technologies) and supplemented with 10% fetal calf serum and 2 mM GlutaMAX (Life Technologies, Carlsbad, CA). Cells were cultured in a humidified incubator at 37°C and 5% CO_2. Three technical replicates of 1×10^7 FT3-7 cells were harvested in lysis buffer [150 mM KCl, 25 mM Tris-HCl (pH 7.4), 5 mM EDTA, 1% Triton X-100, 5 mM DTT, Complete protease inhibitor mixture (Roche), and 100 U/mL RNaseOUT (Life Technologies)]. Lysates were centrifuged for 30 min at 17,000 × g at 4°C and filtered through a 0.22-um filter. Filtrates were incubated with anti-human AGO2 mAb (RN003M, MBL International, Woborn, MA) or isotype control IgG (Abcam, Cambridge, England) at 4°C for 2 h, followed by addition of 30 µL of Protein G Sepharose (GE Healthcare) for 1 h. The Sepaharose beads were washed three times in lysis buffer and RNA extracted using the miRNeasy Mini Kit (Qiagen, Hilden, Germany).

Small RNA real time quantitative PCR (RT-qPCR). Complementary DNA (cDNA) was synthesized using TaqMan MicroRNA Reverse Transcription Kit (Life Technologies) according to the manufacturer's instructions. Real time PCR amplification was performed using TaqMan Universal Master Mix (Life Technologies) on the Bio-Rad CFX96 real time PCR detection system. *U6*, miR-24, let-7a, let-7f, *RNU48*, and *RNU66* were all evaluated as potential housekeeping small RNAs for purposes of normalization. *RNU48* was selected because it was the most consistent across disease groups. RT-qPCR reactions for human samples were performed in triplicate. RT-qPCR reactions for chimpanzee samples were performed in duplicate. The following TaqMan assays were purchased from Life Technologies: miR-122 (product number 4427975; 002245) and *RNU48* or *SNORD48* (product number 4427975; 001006). Primers for the custom TaqMan assays (5′ tRH-^{Gly} and 5′ tRH-^{Val}) were designed using 5′-GCAUUGGUGGUUCAGUGGUAGAAU-UCUCGCCU-3′ for 5′ tRH-^{Gly} and 5′-GUUUCCGUAGUGUAGUGGUUAUCAC-GUUCGCCU-3′ for 5′ tRH^{Val}.

Metabolic Radiolabeling and Measurement of Nascent Protein Synthesis. Huh7 cells were seeded onto the wells of 6-well cell culture plates at a density of 2×10^5 cells/well and incubated overnight to allow cell attachment. Cells were transfected with 50 nM and 100 nM of 5′ tRH^{Gly} (5′-GCAUUGGUGGUUCAGUGGUAGAAU-UCUCGCCU-3′), 5′ tRH^{Val} (5′-GUUUCCGUAGUGUAGUGGUUAUCACGUU-CGCCU-3′), or scramble (5′-GCAUUCACUUGGAUAGUAAAUCCAAGC-UGAA-3′)[21] (all from Integrated DNA Technologies, Coralville, IA) oligonucleotide after replacing cell culture medium with methionine- and cysteine-deficient DMEM (Life Technologies) and cultured for further 12 hrs. Cells were then metabolically radiolabeled for 12 hrs with 200 µCi/well of Express Protein Labeling Mix containing [^{35}S]methionine and [^{35}S]cysteine (PerkinElmer, Waltham, MA) in the presence or absence of 50 µg/ml puromycin and lysed with lysis buffer (20 mM Tris-HCl [pH 7.4] containing 150 mM NaCl, 1% Triton X-100, 0.05% SDS, and 10% glycerol) supplemented with 50 mM NaF, 5 mM Na_3VO_4, and a protease inhibitor cocktail (Complete; Roche, Mannheim, Germany). The protein concentration of cell lysates was determined by the Bio-Rad Protein Assay (Bio-Rad), and 10 µg (total protein) of cell lysates was subjected to SDS-PAGE followed by staining gels with the Sypro Ruby Protein Gel Stain (Bio-Rad, Hercules, CA) and autoradiography.

Immunohistochemistry (IHC). Staining was performed by immunoperoxidase technique with an Envision kit (DAKO Japan). Primary antibodies used were against β-actin (Cell signaling technology, #4967, Beverly, MA) and Human Angiogenin Affinity Purified Polyclonal Ab (R and D Systems, AF265, Minneapolis, MN).

1. Arzumanyan, A., Reis, H. M. & Feitelson, M. A. Pathogenic mechanisms in HBV- and HCV-associated hepatocellular carcinoma. *Nat Rev Cancer* **13**, 123–135 (2013).
2. Perz, J. F., Armstrong, G. L., Farrington, L. A., Hutin, Y. J. & Bell, B. P. The contributions of hepatitis B virus and hepatitis C virus infections to cirrhosis and primary liver cancer worldwide. *J Hepatol* **45**, 529–538 (2006).
3. Hou, W. & Bonkovsky, H. L. Non-coding RNAs in hepatitis C-induced hepatocellular carcinoma: dysregulation and implications for early detection, diagnosis and therapy. *World J Gastroenterol* **19**, 7836–7845 (2013).
4. Xu, X. *et al.* Hepatitis B virus X protein represses miRNA-148a to enhance tumorigenesis. *J Clin Invest* **123**, 630–645 (2013).
5. Chen, Y. *et al.* HCV-induced miR-21 contributes to evasion of host immune system by targeting MyD88 and IRAK1. *PLoS Pathog* **9**, e1003248 (2013).
6. Jopling, C. L., Yi, M., Lancaster, A. M., Lemon, S. M. & Sarnow, P. Modulation of hepatitis C virus RNA abundance by a liver-specific MicroRNA. *Science* **309**, 1577–1581 (2005).
7. Shimakami, T. *et al.* Stabilization of hepatitis C virus RNA by an Ago2-miR-122 complex. *Proc Natl Acad Sci U S A* **109**, 941–946 (2012).
8. Janssen, H. L. *et al.* Treatment of HCV Infection by Targeting MicroRNA. *N Engl J Med* **368**, 1685–1694 (2013).
9. Garcia-Silva, M. R., Cabrera-Cabrera, F. & Güida, M. C. Hints of tRNA-Derived Small RNAs Role in RNA Silencing Mechanisms. *Genes* **3**, 603–614 (2012).
10. Wang, Q. *et al.* Identification and functional characterization of tRNA-derived RNA fragments (tRFs) in respiratory syncytial virus infection. *Mol Ther* **21**, 368–379 (2013).
11. Gong, B. *et al.* Compartmentalized, functional role of angiogenin during spotted fever group rickettsia-induced endothelial barrier dysfunction: evidence of possible mediation by host tRNA-derived small noncoding RNAs. *BMC Infect Dis* **13**, 285 (2013).
12. Saikia, M. *et al.* Angiogenin-Cleaved tRNA Halves Interact with Cytochrome c Protecting Cells from Apoptosis during Osmotic Stress. *Mol Cell Biol* **34**, 2450–63 (2014).
13. Hou, J. *et al.* Identification of miRNomes in human liver and hepatocellular carcinoma reveals miR-199a/b-3p as therapeutic target for hepatocellular carcinoma. *Cancer Cell* **2**, 232–243 (2011).
14. Spaniel, C., Honda, M., Selitsky, S. R. & Yamane, D. microRNA-122 abundance in hepatocellular carcinoma and non-tumor liver tissue from Japanese patients with persistent HCV versus HBV infection. *PloS One* **8**, e76867 (2013).
15. Bartel, D. P. MicroRNAs: target recognition and regulatory functions. *Cell* **136**, 215–233 (2009).
16. Chan, P. P. & Lowe, T. M. GtRNAdb: a database of transfer RNA genes detected in genomic sequence. *Nucleic Acids Res* **37**, D93–97 (2009).
17. Kozomara, A. & Griffiths-Jones, S. miRBase: annotating high confidence microRNAs using deep sequencing data. *Nucleic Acids Res* **42**, D68–73 (2014).
18. Lanford, R. E., Lemon, S. M. & Walker, C. in *Hepatitis C Antiviral Drug Discovery & Development* (eds He, Y. & Tan, T.) 99–132 (Horizons Scientific Press, 2011).
19. Asabe, S. *et al.* The size of the viral inoculum contributes to the outcome of hepatitis B virus infection. *J Virol* **83**, 9652–9662 (2009).
20. Fu, H. *et al.* Stress induces tRNA cleavage by angiogenin in mammalian cells. *FEBS Lett* **583**, 437–442 (2009).
21. Yamasaki, S., Ivanov, P., Hu, G.-F. & Anderson, P. Angiogenin cleaves tRNA and promotes stress-induced translational repression. *J Cell Biol* **185**, 35–42 (2009).
22. Wang, Q. *et al.* Identification and functional characterization of tRNA-derived RNA fragments (tRFs) in respiratory syncytial virus infection. *Mol Ther* **21**, 368–379 (2013).
23. Gong, B. *et al.* Compartmentalized, functional role of angiogenin during spotted fever group rickettsia-induced endothelial barrier dysfunction: evidence of possible mediation by host tRNA-derived small noncoding RNAs. *BMC Infect Dis* **13**, 285 (2013).
24. Mishima, E. *et al.* Conformational Change in Transfer RNA Is an Early Indicator of Acute Cellular Damage. *J Am Soc Nephrol* **25**, 2316–26 (2014).
25. Ivanov, P., Emara, M. M., Villen, J., Gygi, S. P. & Anderson, P. Angiogenin-induced tRNA fragments inhibit translation initiation. *Mol Cell* **43**, 613–623 (2011).
26. Emara, M. M. *et al.* Angiogenin-induced tRNA-derived stress-induced RNAs promote stress-induced stress granule assembly. *J Biol Chem* **285**, 10959–10968 (2010).
27. Dhahbi, J. M. *et al.* 5′ tRNA halves are present as abundant complexes in serum, concentrated in blood cells, and modulated by aging and calorie restriction. *BMC Genomics* **14**, 298 (2013).
28. Vojtech, L. *et al.* Exosomes in human semen carry a distinctive repertoire of small non-coding RNAs with potential regulatory functions. *Nucleic Acids Res* **42**, 7290–7304 (2014).
29. Garcia-Silva, M. R. *et al.* Gene Expression Changes Induced by Trypanosoma cruzi Shed Microvesicles in Mammalian Host Cells: Relevance of tRNA-Derived Halves. *Biomed Res Int* **2014**, 305239 (2014).
30. Fu, H. *et al.* Stress induces tRNA cleavage by angiogenin in mammalian cells. *FEBS Lett* **583**, 437–442 (2009).
31. Yamasaki, S., Ivanov, P., Hu, G.-F. & Anderson, P. Angiogenin cleaves tRNA and promotes stress-induced translational repression. *J Biol Chem* **185**, 35–42 (2009).
32. Gao, X. & Xu, Z. Mechanisms of action of angiogenin. *Acta Biochim Biophys Sin (Shanghai)* **40**, 619–624 (2008).
33. Pizzo, E. *et al.* Ribonuclease/angiogenin inhibitor 1 regulates stress-induced subcellular localization of angiogenin to control growth and survival. *J Cell Sci* **126**, 4308–4319 (2013).
34. Saxena, S. K., Rybak, S. M., Davey, R. T., Youle, R. J. & Ackerman, E. J. Angiogenin is a cytotoxic, tRNA-specific ribonuclease in the RNase A superfamily. *J Biol Chem* **267**, 21982–21986 (1992).
35. Mazzanti, R. *et al.* Chronic viral hepatitis induced by hepatitis C but not hepatitis B virus infection correlates with increased liver angiogenesis. *Hepatology* **25**, 229–234 (1997).
36. Messerini, L., Novelli, L. & Comin, C. E. Microvessel density and clinicopathological characteristics in hepatitis C virus and hepatitis B virus related hepatocellular carcinoma. *J Clin Pathol* **57**, 867–871 (2004).
37. Walker, C. M. Comparative features of hepatitis C virus infection in humans and chimpanzees. *Springer Semin Immunopathol* **19**, 85–98 (1997).
38. Mason, W. S. *et al.* Detection of clonally expanded hepatocytes in chimpanzees with chronic hepatitis B virus infection. *J Virol* **83**, 8396–8408 (2009).
39. Jackman, J. E. & Alfonzo, J. D. Transfer RNA modifications: nature's combinatorial chemistry playground. *Wiley Interdisciplin Rev RNA* **4**, 35–48 (2013).

40. Kozomara, A. & Griffiths-Jones, S. miRBase: annotating high confidence microRNAs using deep sequencing data. *Nucleic Acids Res* **42**, D68–73 (2014).
41. Langmead, B., Trapnell, C., Pop, M. & Salzberg, S. L. Ultrafast and memory-efficient alignment of short DNA sequences to the human genome. *Genome Biol* **10**, R25 (2009).
42. David, M., Dzamba, M., Lister, D., Ilie, L. & Brudno, M. SHRiMP2: sensitive yet practical short read mapping. *Bioinformatics* **27**, 1011–2 (2011).
43. Larkin, M. A., Blackshields, G., Brown, N. P. & Chenna, R. Clustal W and Clustal X version 2.0. *Bioinformatics* **23**, 2947–2948 (2007).

Acknowledgments

This work was supported by grants from the National Institutes of Health: R00-DK091318 (P.S.); R01-AI095690 and R01-CA164029 (S.M.L); T32-GM067553 and T32-AI007419 (S.R.S). The Southwest National Primate Research Center is supported by a grant from the NIH Office of Research Infrastructure Programs/OD P51 OD011133), and by Research Facilities Improvement Program Grants C06 RR 12087 and C06 RR016228.

Author contributions

The experiments were designed by S.R.S., P.S. and S.M.L. The data were analyzed by S.R.S., J.B., T. Shirasaki, M.H., P.S. and S.M.L. Experiments were performed by S.R.S., D.Y., T.M., E.E.F., B.G. and T. Shirasaki. M.H., T. Shimakami, S.K., R.E.L., S.M.L. and P.S. contributed resources. The manuscript was written by S.R.S., P.S. and S.M.L.

Additional information

Supplementary information accompanies this paper at http://www.nature.com/scientificreports

Competing financial interests: The authors declare no competing financial interests.

How to cite this article: Selitsky, S.R. *et al.* Small tRNA-derived RNAs are increased and more abundant than microRNAs in chronic hepatitis B and C. *Sci. Rep.* **5**, 7675; DOI:10.1038/srep07675 (2015).

HEPATOLOGY
Official Journal of the American Association for the Study of Liver Diseases

Gd-EOB-DTPA-Enhanced Magnetic Resonance Imaging and Alpha-Fetoprotein Predict Prognosis of Early-Stage Hepatocellular Carcinoma

Taro Yamashita,[1,2] Azusa Kitao,[3] Osamu Matsui,[3] Takehiro Hayashi,[2] Kouki Nio,[2] Mitsumasa Kondo,[2] Naoki Ohno,[4] Tosiaki Miyati,[4] Hikari Okada,[2] Tatsuya Yamashita,[2] Eishiro Mizukoshi,[2] Masao Honda,[2] Yasuni Nakanuma,[5] Hiroyuki Takamura,[6] Tetsuo Ohta,[6] Yasunari Nakamoto,[7] Masakazu Yamamoto,[8] Tadatoshi Takayama,[9] Shigeki Arii,[10] XinWei Wang,[11] and Shuichi Kaneko[2]

The survival of patients with hepatocellular carcinoma (HCC) is often individually different even after surgery for early-stage tumors. Gadolinium ethoxybenzyl diethylenetriamine pentaacetic acid (Gd-EOB-DTPA)-enhanced magnetic resonance imaging (MRI) has been introduced recently to evaluate hepatic lesions with regard to vascularity and the activity of the organic anion transporter OATP1B3. Here we report that Gd-EOB-DTPA-enhanced MRI (EOB-MRI) in combination with serum alpha-fetoprotein (AFP) status reflects the stem/maturational status of HCC with distinct biology and prognostic information. Gd-EOB-DTPA uptake in the hepatobiliary phase was observed in ~15% of HCCs. This uptake correlated with low serum AFP levels, maintenance of hepatocyte function with the up-regulation of *OATP1B3* and *HNF4A* expression, and good prognosis. By contrast, HCC showing reduced Gd-EOB-DTPA uptake with high serum AFP levels was associated with poor prognosis and the activation of the oncogene *FOXM1*. Knockdown of *HNF4A* in HCC cells showing Gd-EOB-DTPA uptake resulted in the increased expression of *AFP* and *FOXM1* and the loss of *OATP1B3* expression accompanied by morphological changes, enhanced tumorigenesis, and loss of Gd-EOB-DTPA uptake *in vivo*. HCC classification based on EOB-MRI and serum AFP levels predicted overall survival in a single-institution cohort (n = 70), and its prognostic utility was validated independently in a multi-institution cohort of early-stage HCCs (n = 109). *Conclusion*: This noninvasive classification system is molecularly based on the stem/maturation status of HCCs and can be incorporated into current staging practices to improve management algorithms, especially in the early stage of disease. (HEPATOLOGY 2014;60:1674-1685)

Liver cancer is the fifth most commonly diagnosed cancer and the second most frequent cause of cancer death in men worldwide.[1] Among primary liver cancers, hepatocellular carcinoma (HCC) represents the major histological subtype, accounting for 70-86% of cases of primary liver cancer.[1] Several staging systems are currently available for HCC classification and include Tumor Node

Abbreviations: AFP, alpha-fetoprotein; BCLC, Barcelona Clinic Liver Cancer; EOB-MRI, gadolinium ethoxybenzyl diethylenetriamine pentaacetic acid-enhanced magnetic resonance imaging; FOXM1, forkhead box protein M1; Gd-EOB-DTPA, gadolinium ethoxybenzyl diethylenetriamine pentaacetic acid; HCC, hepatocellular carcinoma; HNF4α, hepatocyte nuclear factor 4 alpha; IHC, immunohistochemistry; MRI, magnetic resonance imaging; NOD/SCID, nonobese diabetic, severe combined immunodeficient; OATPs, organic anion transporting polypeptides; qRT-PCR, quantitative reverse-transcription polymerase chain reaction; SI, signal intensity; TNM, tumor node metastasis.

From the [1]Department of General Medicine, Kanazawa University Graduate School of Medical Science, Kanazawa, Ishikawa, Japan; [2]Department of Gastroenterology, Kanazawa University Graduate School of Medical Science, Kanazawa, Ishikawa, Japan; [3]Department of Radiology, Kanazawa University Graduate School of Medical Science, Kanazawa, Ishikawa, Japan; [4]Faculty of Health Sciences, Institute of Medical, Pharmaceutical and Health Sciences, Kanazawa University, Kanazawa, Ishikawa, Japan; [5]Department of Pathology, Kanazawa University Graduate School of Medical Science, Kanazawa, Ishikawa, Japan; [6]Department of Gastroenterologic Surgery, Kanazawa University Graduate School of Medical Science, Kanazawa, Ishikawa, Japan; [7]Second Department of Internal Medicine, Fukui University School of Medicine, Fukui, Japan; [8]Department of Surgery, Institute of Gastroenterology, Tokyo Women's Medical University, Tokyo, Japan; [9]Department of Digestive Surgery, Nihon University School of Medicine, Tokyo, Japan; [10]Department of Hepato-Biliary-Pancreatic Surgery, Tokyo Medical and Dental University, Tokyo, Japan; [11]Laboratory of Human Carcinogenesis, Center for Cancer Research, National Cancer Institute, Bethesda, MD, USA.

Received September 19, 2013; accepted February 20, 2014.

Metastasis (TNM) and Barcelona Clinic Liver Cancer (BCLC) staging, which are based on tumor number and size, vascular invasion, metastatic status, hepatic reserve, and performance status.[2] These systems can provide an approximate estimate of patients' survival, but patients diagnosed at the same disease stage sometimes show a different prognosis. This is most likely because these systems do not include an assessment of the malignant phenotype of the tumor, which would be especially important in those patients diagnosed at the early stage of disease. To overcome these limitations, gene expression profiling technologies have been applied to classify HCC. In particular, the stemness of HCC is currently of great interest because its gene expression profile reflects the malignant nature of the tumor.[3-7] However, the application of these new technologies still needs to be validated externally prior to their implementation in clinical practice.

The hallmark of HCC diagnosis has been image analysis based on vascularity. Gadolinium ethoxybenzyl diethylenetriamine pentaacetic acid (Gd-EOB-DTPA) is a liver-specific magnetic resonance imaging (MRI) contrast agent introduced specifically to improve the detection of liver lesions.[8] Gd-EOB-DTPA-enhanced MRI (EOB-MRI) has been used to evaluate liver tumors in Europe since 2004, in the USA and Japan since 2008, and in China since 2010. Gd-EOB-DTPA is characterized by its rapid and specific uptake by hepatocytes by way of organic anion transporting polypeptides (OATPs) expressed in the sinusoidal membrane. Therefore, Gd-EOB-DTPA uptake in the liver is considered to reflect hepatocyte function.[9] Among OATP1A2, 1B1, 1B3, and 2B1, only OATP1B3 expression was found to correlate with the enhancement ratio on EOB-MRI, indicating that it transports Gd-EOB-DTPA into HCC cells.[10] It is generally accepted that ~85% of HCCs show hypointensity in the hepatobiliary phase of EOB-MRI compared to the noncancerous background liver, with a reduction of OATP1B3 protein or *OATP1B3* gene expression in the tumor.[10,11] However, atypical Gd-EOB-DTPA uptake in the hepatobiliary phase is observed in the remaining 15% of HCCs, and the molecular phenotype and clinical features of these HCCs remain to be elucidated.

We hypothesized that EOB-MRI findings may vary in different tumor subtypes with distinct biology. Therefore, in this study we evaluated the molecular profiles of HCCs in a single-institute cohort determined from the EOB-MRI findings using quantitative reverse-transcription polymerase chain reaction (qRT-PCR), microarray, and immunohistochemistry (IHC) analyses. To clarify the clinical utility of the EOB-MRI findings, we also evaluated the prognosis of a multicenter cohort of patients with early-stage HCC who underwent radical resection.

Materials and Methods

Patients. A total of 417 patients who received surgical resection for HCC were enrolled in this study. Seventy patients underwent EOB-MRI for the diagnosis of HCC and received surgical resection at Kanazawa University Hospital from 2008 to 2011. Survival analysis was performed in this single-institute cohort (Cohort 1) and prognosis was evaluated every 6 months. The final evaluation of survival was performed in October 2011. From these 70 patients, 62 tumor and nontumor samples were snap-frozen in liquid nitrogen and used for qRT-PCR.

For microarray analysis, we assessed 238 patients who received surgical resection of HCC at the Liver Cancer Institute of Fudan University. EOB-MRI was not performed in these patients because Gd-EOB-DTPA had not yet been introduced in China. Their clinicopathologic characteristics and prognostic data have been described previously.[12]

To evaluate the survival of early-stage HCCs, we enrolled 109 patients who received EOB-MRI and surgical resection at Tokyo Medical and Dental University Hospital, Tokyo Women's Medical University Hospital, Nihon University School of Medicine Itabashi Hospital, Niigata University Medical & Dental Hospital, Hyogo College of Medicine Hospital, or Kurume

Supported by Health and Labor Sciences Research Grants for "Development of novel molecular markers and imaging modalities for earlier diagnosis of hepatocellular carcinoma," Grants from the Ministry of Education, Culture, Sports, Science, and Technology of Japan, the National Cancer Center Research and Development Fund (23-B-5), and the Intramural Research Program Grant (Z01 BC 010313) of the Center for Cancer Research, US National Cancer Institute.

Address reprint requests to: Taro Yamashita, M.D., Ph.D., Assistant Professor, Department of Gastroenterology/General Medicine, Kanazawa University Graduate School of Medical Science, 13-1 Takara-Machi, Kanazawa, Ishikawa 920-8641, Japan. E-mail: taroy@m-kanazawa.jp; fax: +81-76-234-4250.

View this article online at wileyonlinelibrary.com.
DOI 10.1002/hep.27093
Potential conflict of interest: Dr. Matsui is on the speakers' bureau for Bayer.

University Hospital from 2008 to 2009 (Cohort 2). The prognosis of these patients was evaluated every year, and the final evaluation of survival was performed in February 2012.

This study was approved by the Institutional Review Board at each study center and all patients provided written informed consent.

EOB-MRI. EOB-MRI was performed before surgical resection using a 1.5 or 3.0 Tesla MRI system with a fat-suppressed 2D or 3D gradient echo T1-weighted sequence (relaxation time / echo time [TR/TE] = 3.2-3.6/1.6-2.3 ms, flip angle 10-15°, field of view 33-42 cm, matrix 128-192 × 256-512, slice thickness 4.0-8.0 mm). A dose of 0.025 mmol/kg Gd-EOB-DTPA (Primovist; Bayer Schering Pharma, Berlin, Germany) was injected intravenously and the hepatobiliary phase was obtained at 15-20 minutes after the injection.

All abdominal MRI data of the HCC patients were generated at Kanazawa University Hospital and image analysis was performed retrospectively by two radiologists (A.K. and O.M.) without knowledge of the clinical and pathological results. The signal intensity (SI) of the tumor was measured within the region of interest, which was determined as the maximum oval area at the largest section of the tumor. The SI of the adjacent background liver was also measured within a region of interest of the same size, while avoiding large vessels. The nodules were classified into the two following types: hypointense HCC, which was defined as showing a lower SI than that of the surrounding liver (tumor SI / background SI <1.0) in the hepatobiliary phase, and hyperintense HCC, which was defined as showing an equal or higher SI (tumor SI / background SI ≥1.0).

For the mouse study, EOB-MRI was performed using a 0.4 T MRI system with a fat-suppressed 3D gradient echo T1-weighted sequence (TR/TE = 66.5/4.0 ms, flip angle 40°, field of view 10 cm, matrix 224 × 192, slice thickness 1.0 mm). A dose of 0.025 mmol/kg Gd-EOB-DTPA (Bayer Schering Pharma) was injected through the tail vein, and the hepatobiliary phase was obtained at 12-20 minutes after the injection.

Xenotransplantation of Primary HCC in Immunodeficient Mice and* HNF4A *Knockdown. Primary HCC tissue was dissected and digested in 1 mg/mL type 4 collagenase solution (Sigma-Aldrich Japan, Tokyo, Japan) at 37°C for 15-30 minutes. Contaminated red blood cells were lysed with an ammonium chloride solution (STEMCELL Technologies, Vancouver, BC, Canada) on ice for 5 minutes. $CD45^+$ leukocytes and annexin V^+ apoptotic cells were removed by an autoMACS-pro cell separator and magnetic beads (Miltenyi Biotec, Tokyo, Japan). The cells were suspended 1:1 in 200 μL Dulbecco's modified Eagle's medium (DMEM) and Matrigel (BD Biosciences) and injected subcutaneously into 6-week-old NOD/SCID mice (NOD/NCrCRl-*Prkdc*^{scid}) purchased from Charles River Laboratories (Wilmington, MA). EOB-MRI was performed to evaluate Gd-EOB-DTPA uptake in the subcutaneous tumor at the hepatobiliary phase, and the subcutaneous tumor was dissected and digested as described above, and subsequently cultured in DMEM. *HNF4A* knockdown was performed using pGFP-V-RS vectors (OriGene Technologies, Rockville, MD), allowing stable delivery of the short hairpin RNA (shRNA) expression cassette against *HNF4A* or scramble sequence into host cells by way of a replication-deficient retrovirus. Infected HCC cells were grown in DMEM containing 1 μg/mL puromycin (Sigma-Aldrich Japan) for 7 days to establish stable shRNA-expressing HCC cells. Western blotting and immunofluorescence analyses were performed using an antihuman HNF4α C11F12 antibody (Cell Signaling Technology, Danvers, MA) and a mouse monoclonal antihuman OATP1B3 MDQ/5F260 antibody (Novus Biologicals, Littleton, CO), essentially as described previously.[13] Control or Sh-HNF4A-transfected HCC cells were injected subcutaneously into NOD/SCID mice, and tumor volume and survival were evaluated every 2-3 days. The protocol was approved by the Kanazawa University Animal Care and Use Committee and the Kanazawa University Genetic Modification Experiment Committee.

Microarray Analysis. The 238 HCC cases from the Liver Cancer Institute of Fudan University with available microarray data and clinicopathologic and prognostic data have been described previously.[12] BRB-ArrayTools software (v. 3.8.1) was used for class comparison analysis. Hierarchical clustering analysis was performed with Genesis software (v. 1.6.0 beta). Canonical pathway and transcription factor analyses were performed using MetaCore software (http://www.genego.com). Interaction network analysis was performed using Ingenuity Pathway Analysis software (http://www.ingenuity.com).

qRT-PCR Analysis. Total RNA was extracted using an RNeasy Mini Kit (Qiagen, Valencia, CA) according to the manufacturer's instructions. The expression of selected genes was determined in triplicate using the Applied Biosystems 7900HT Sequence Detection System (Applied Biosystems, Foster City, CA) and the $-\Delta\Delta CT$ method. The following probes were used: *AFP*, Hs00173490_m1; *FOXM1*, Hs01073586_m1; *OATP1B3*, Hs00251986_m1; *CYP3A4*, Hs00430021_m1; and *18S*, Hs99999901_s1 (Applied Biosystems).

IHC Analysis. IHC was performed using Envision+ kits (Dako Japan, Tokyo, Japan) as described previously.[14] Mouse monoclonal antihuman Ki-67 antigen MIB-1 (Dako Japan), mouse monoclonal antihuman OATP1B3 MDQ/5F260 (Novus Biologicals), rabbit monoclonal antihuman HNF4α C11F12 (Cell Signaling Technology), mouse monoclonal antihuman FOXM1 0.T.181 (Abcam, Cambridge, MA), mouse monoclonal antihuman glypican-3 1G12 (BioMosaics, Burlington, VT), and mouse monoclonal antiglutamine synthetase clone GS-6 (Millipore, Billerica, MA) antibodies were used. The staining area and intensities were evaluated in each sample and graded from 0-3 (0, 0-5%; 1, 5-25%; 2, 25-50%; 3, >50%) and 0-2 (0, negative; 1, weak; 2, strong), respectively. The sum of the area and intensity scores of each marker (IHC score) were calculated. Samples were defined as marker-high (IHC score $\geq$3) or -low (IHC score $\leq$2). The Ki-67 labeling index was calculated as described previously.[14]

Statistical Analysis. Mann-Whitney, χ^2, Fisher's exact, and Kruskal-Wallis tests were used to compare the clinicopathologic characteristics and gene expression data. The correlation of the gene expression data was evaluated by Spearman's rank correlation coefficient. Kaplan-Meier survival analysis with the log-rank test was performed to compare patient survival. All analyses were performed using GraphPad Prism software v. 5.0.1 (GraphPad Software, San Diego, CA).

Results

EOB-MRI Findings and Molecular Characteristics of HCC. Nine of the 70 HCC cases (12.9%) in Cohort 1 were diagnosed with hyperintense HCC on EOB-MRI (Fig. 1A). Analysis of the clinicopathologic characteristics of hyper- or hypointense HCCs revealed that hyperintense HCCs were significantly associated with low serum alpha-fetoprotein (AFP) levels (Table 1). There was no significant difference between hyper- and hypointense HCCs in terms of other factors, including tumor size, number, TNM and BCLC stages, surgical procedures, and elapsed time between MRI and surgery. We confirmed the overexpression of OATP1B3, a transporter responsible for the uptake of Gd-EOB-DTPA in hepatocytes, in hyperintense HCCs by qRT-PCR and IHC (Fig. 1B).

To understand the transcriptomic characteristics of HCCs overexpressing *OATP1B3*, we analyzed the microarray data of an additional 238 HCC cases.[12] *OATP1B3*-high and -low HCCs were defined as HCCs with a T/N ratio $\geq$1.0 and <1.0, respectively, as used for the evaluation of hyperintense HCCs (tumor SI / background SI $\geq$1.0). The frequency of *OATP1B3*-high HCCs was 15.1% (36 of the 238 HCC cases), almost comparable to the frequency of hyperintense HCCs reported thus far. Class-comparison analysis yielded a total of 974 genes that were differentially expressed between *OATP1B3*-high and -low HCCs ($P < 0.001$). Hierarchical cluster analysis of this 974 gene set (*OATP1B3* gene signature) separated HCCs into two branches (B1 and B2) (Fig. 1C). Thirty-four of the 36 *OATP1B3*-high HCCs (blue box) were classified in the left branch (B1), while *OATP1B3*-low HCCs were clustered in both branches. The prognosis of HCC patients clustered in B1 was significantly better than those clustered in B2 ($P = 0.02$) (Supporting Fig. S1). Genes associated with mature hepatocyte function such as *ALB* and *CYP3A4* were significantly up-regulated in the HCCs clustered in B1, and the known hepatic stem/progenitor markers *KRT19* and *EPCAM*, as well as the G1/S cell cycle marker *MKI67*, were significantly up-regulated in the HCCs clustered in B2 (Fig. 1D).

Pathway analysis indicated that *OATP1B3*-high HCCs showed maintenance of mature hepatocyte function and decreased cell proliferation and Wnt signaling (Fig. 1E), which are known to be activated during liver development and regeneration.[15] Transcription factor analysis identified eight genes (*HNF4A, NFIA, NR3C1, NR1I3, ESR1, NR1H3, MLXIPL*, and *NFE2L2*) as candidate transcription factors that were significantly activated in *OATP1B3*-high HCCs ($P < 0.005$) (Fig. 1F). These transcription factors are known to play a pivotal role in liver development and in the regulation of hepatocyte functions including lipid, bile, carbohydrate, and xenobiotic metabolism.[16] By contrast, only one gene (*FOXM1*) was identified as a candidate transcription factor activated in *OATP1B3*-low HCCs. The forkhead box M1 (FOXM1) transcription factor is known to be activated during liver regeneration and regulation of the cell cycle.[17] We investigated the expression of the two transcription factors most strongly activated (*HNF4A* encoding hepatocyte nuclear factor 4 alpha [HNF4α]) or inactivated (*FOXM1*) in hyperintense HCCs (Fig. S2) and validated the results using microarray analyses (Fig. 2A,B).

Although the microarray data revealed distinct molecular portraits associated with liver development and the maturation programs present in hyper- and hypointense HCCs, hierarchical cluster analysis further indicated that a subset of hypointense HCCs (corresponding to the *OATP1B3*-low HCCs clustered in B1)

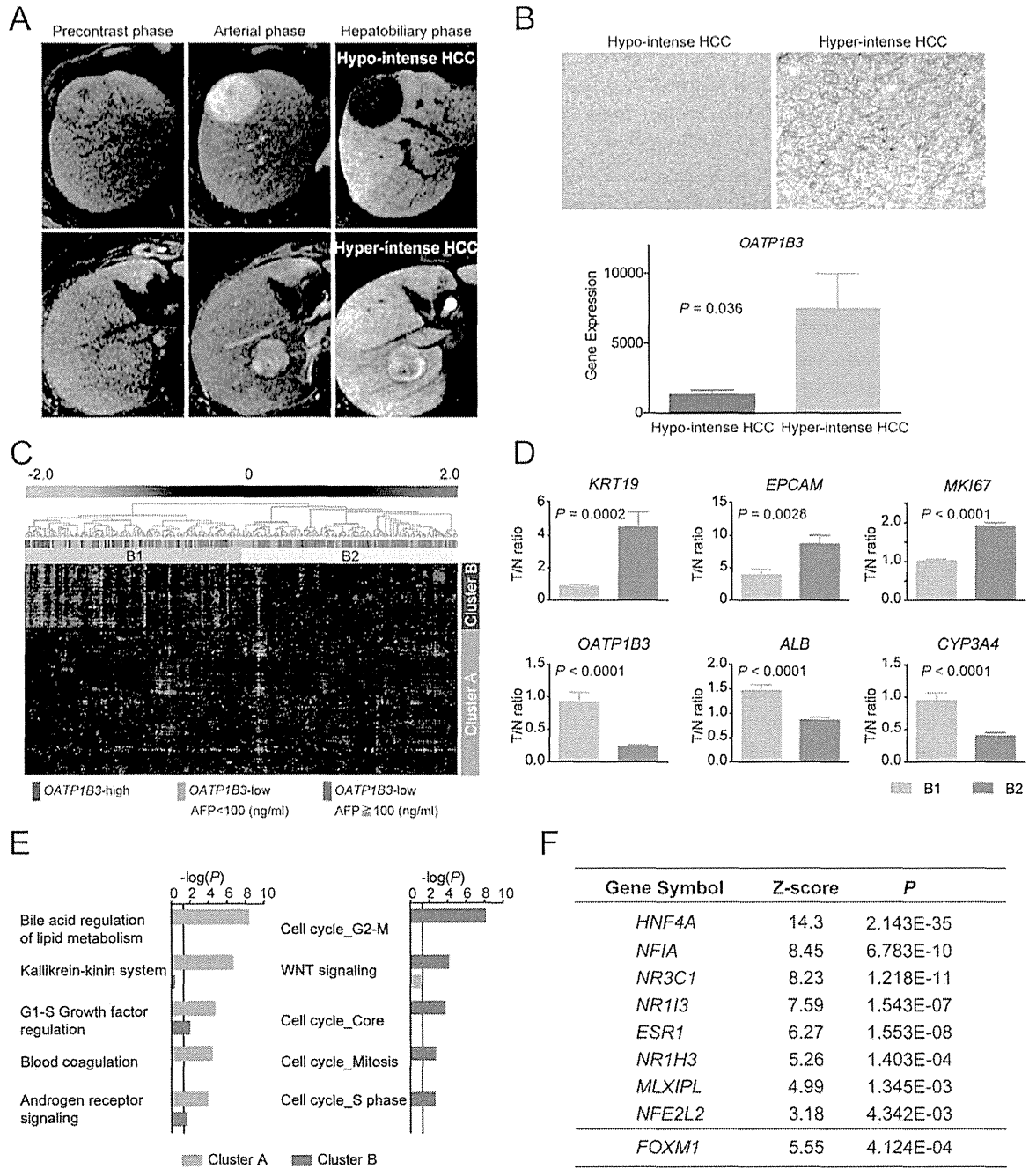

F

Gene Symbol	Z-score	P
HNF4A	14.3	2.143E-35
NFIA	8.45	6.783E-10
NR3C1	8.23	1.218E-11
NR1I3	7.59	1.543E-07
ESR1	6.27	1.553E-08
NR1H3	5.26	1.403E-04
MLXIPL	4.99	1.345E-03
NFE2L2	3.18	4.342E-03
FOXM1	5.55	4.124E-04

Fig. 1. Molecular profiles of HCCs corresponding to the EOB-MRI findings. (A) Representative MRI scans of hypo- and hyperintense HCCs in the precontrast, arterial, and hepatobiliary phases. The T/N signal intensity ratios of the images in the hepatobiliary phase were 0.47 (upper panel) and 1.07 (lower panel). (B) Upper panel: Representative photomicrographs of IHC staining with an anti-OATP1B3 antibody in hypo- and hyperintense HCCs. Lower panel: *OATP1B3* expression in hypo- and hyperintense HCCs. (C) The expression patterns of *OATP1B3* signatures in *OATP1B3*-high (blue box), *OATP1B3*-low AFP-low (<100 ng/mL) (orange box), and *OATP1B3*-low AFP-high (≥100 ng/mL; red box) after hierarchical clustering of genes and samples, shown as a heat map image. Red indicates a high expression level; green indicates a low expression level. *OATP1B3*-high HCCs and *OATP1B3*-low AFP-high HCCs were clustered in B1 (green bar) and B2 (yellow bar), respectively. (D) Representative expression of genes in clusters A (*KRT19, EPCAM*, and *MKI67*) and B (*OATP1B3, ALB*, and *CYP3A4*). The green and orange bars indicate HCCs clustered in B1 and B2, respectively. (E) The activated pathways are identified in clusters A (orange bar) and B (blue bar). (F) Genes encoding transcription factors activated or inactivated in *OATP1B3*-high HCCs.

might show similar gene expression profiles to those observed in hyperintense HCCs. Since serum AFP levels are reportedly related to the stem/maturation subtypes of HCCs with different gene expression profiles,[12] we analyzed the characteristics of *OATP1B3*-low HCCs in 238 cases according to serum AFP levels. Interestingly, *OATP1B3*-low HCCs assigned to the left branch (B1) had low serum AFP

Table 1. Characteristics of HCCs Classified by EOB-MRI in Cohorts 1 and 2

Characteristics	Cohort 1			Cohort 2		
	Hyperintense (n = 9)	Hypointense (n = 61)	P*	Hyperintense (n = 9)	Hypointense (n = 100)	P*
Age (years, mean ± SE)	66.2 ± 3.6	64.6 ± 1.2	0.21	67.2 ± 2.0	66.2 ± 1.0	1.0
Sex (male/female)	7/2	44/17	0.72	9/0	79/21	0.13
Etiology (HBV/HCV/other)	2/3/4	14/23/24	0.95	1/6/0/2	22/56/2/20	0.52
Liver cirrhosis (yes/no)	5/4	33/28	0.94	2/7	42/58	0.25
AFP (ng/mL, mean ± SE)	12.4 ± 1.9	2,157 ± 866	0.03	7.0 ± 2.2	188.4 ± 74	0.03
Histologic grade†						
I–II	1	12		2	16	
II–III	8	38		7	74	
III–IV	0	11	0.25	0	10	0.57
Tumor size (cm, mean ± SE)	4.0 ± 0.9	4.4 ± 0.4	0.79	3.3 ± 0.4	2.6 ± 0.1	0.09
Tumor number (single/multiple)	7/2	48/13	0.95	8/1	86/14	0.81
Macroscopic portal vein invasion (yes/no)	1/8	5/56	0.58	0/9	0/100	
Microscopic portal vein invasion (yes/no)	2/7	27/34	0.21	0/9	11/89	0.59
Tumor-node-metastasis classification (I/II/III)	6/2/1	29/28/4	0.40	7/2/0	75/25/0	0.85
BCLC stage (0/A/B/C)	0/7/1/1	4/30/22/5	0.34	0/9/0/0	27/73/0/0	0.07
Elapsed time between MRI and surgery (days, mean ± SE)	47.0 ± 8.4	51.5 ± 3.2	0.73	17.3 ± 5.0	20.6 ± 3.0	0.50
Surgical procedure (partial resection or segmentectomy/ lobectomy or extended lobectomy)	6/3	35/26	0.60	8/1	86/14	1.0

*Mann-Whitney test, Fisher's exact test, or χ^2 test.
†Edmondson-Steiner.

levels (<100 ng/mL: orange box, Fig. 1C), while the majority of AFP-high (≥100 ng/mL) HCCs (red box, Fig. 1C) were clustered in the right branch (B2). Consistently, the *OATP1B3* gene signature significantly predicted the serum AFP status of 238 HCCs ($P < 0.05$) (Tables S1-3).

OATP1B3 and AFP Expression in HCC Subtypes Related to Stem/Maturational Status. Molecular profiling of tissue samples may be useful for predicting the survival of HCC patients, as reported previously.[18,19] However, such an approach should be established before being applied routinely in a clinical setting. The above data prompted us to hypothesize that EOB-MRI findings and serum AFP levels, in place of molecular profiling techniques, have the potential to categorize HCCs (EOB-AFP classification), thus serving as predictors of survival. We categorized HCCs into three groups (class A: hyperintense HCC, class B: hypointense and AFP-low [<100 ng/mL] HCC, and class C: hypointense and AFP-high [≥100 ng/mL] HCC). The clinicopathologic characteristics of patients with class A, B, and C HCCs in Cohort 1 are shown in Table S4.

We investigated the expression of HNF4α and FOXM1 as well as the G1/S marker Ki-67 by IHC according to the EOB-AFP classification system in Cohort 1 (Fig. 2C). HNF4α was most abundantly expressed in class A HCCs, but its expression was decreased in class B and C HCCs. By contrast, the expression of FOXM1 and Ki-67 was highest in class C HCCs, significantly decreased in class B HCCs, and not detected in class A HCCs. The mean Ki-67 labeling indices in class A, B, and C HCCs were 2.8%, 9.4%, and 18.2%, respectively ($P < 0.0001$) (Fig. 2D). The differences in FOXM1 and HNF4α expression among class A, B, and C HCCs were statistically significant (Fig. 2E).

We further investigated the expression of five markers (glypican 3, GPC-3; lymphatic vessel endothelial hyaluronan receptor 1, LYVE-1; survivin; heat shock 70 kDa protein, HSP70; and glutamine synthetase, GS), known to be differentially expressed between dysplastic nodule and well-differentiated HCC,[20,21] to clarify if the molecular alterations in early-stage hepatocarcinogenesis can be detected differentially in EOB-AFP class A, B, and C HCCs. IHC analysis suggested no differential expression of LYVE-1, survivin, and HSP70 among the EOB-AFP classes (data not shown). Interestingly, GS was most abundantly expressed in class A HCCs, and its expression was relatively decreased in class B and C HCCs with borderline significance ($P = 0.06$) (Fig. S3A,B). In contrast, GPC-3 expression was highest in class C HCCs and relatively decreased in class A and B HCCs with statistical significance ($P = 0.03$). We investigated the microarray data of 238 independent HCC cases and validated the positive correlation between *OATP1B3* and *GLUL* (encoding GS) and the weak negative correlation between *OATP1B3* and *GPC3* (encoding GPC-3).

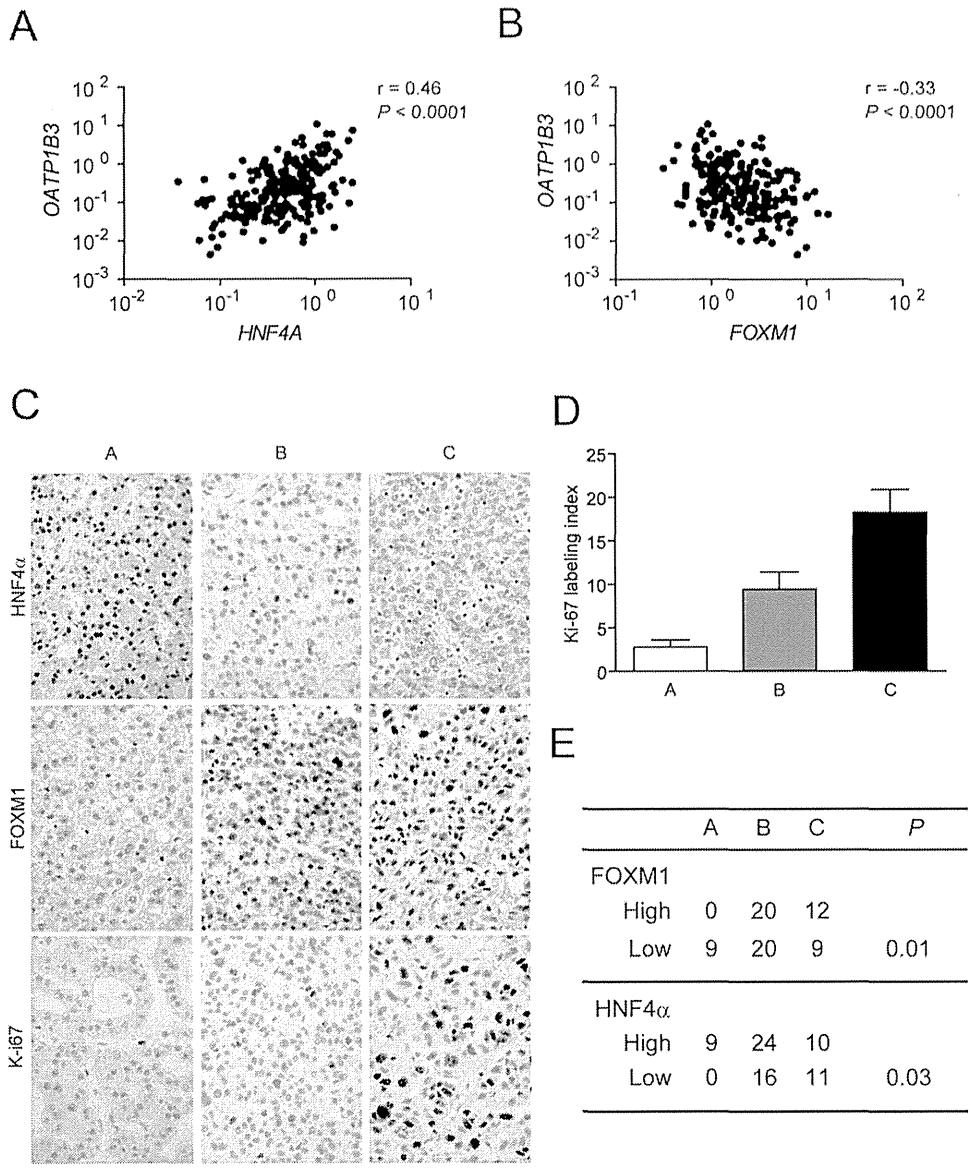

E

	A	B	C	P
FOXM1				
High	0	20	12	
Low	9	20	9	0.01
HNF4α				
High	9	24	10	
Low	0	16	11	0.03

Fig. 2. Transcriptional programs of HCCs corresponding to the EOB-MRI findings and serum AFP. (A,B) Scatterplot analyses of the microarray data of 238 HCCs. (C) Representative photomicrographs of IHC staining with anti-HNF4α, anti-FOXM1, and anti-Ki-67 antibodies in class A, B, and C HCCs, according to the EOB-AFP classification. (D) Ki-67 labeling index in class A, B, and C HCCs. (E) Summary of FOXM1 and HNF4α expression in class A, B, and C HCCs.

Regulation of Gd-EOB-DTPA Uptake and Tumorigenic Capacity by HNF4α in Hyperintense HCC. Microarray and IHC analyses suggested the activation of transcription factor HNF4α in hyperintense HCC, but its role in the maintenance of hepatocyte function and Gd-EOB-DTPA uptake has not yet been clarified. To directly explore the role of HNF4α in Gd-EOB-DTPA uptake and tumorigenic capacities, we transplanted tumor cells from hyper- and hypointense primary HCC specimens into NOD/SCID mice (Fig. 3A). We confirmed on EOB-MRI that Gd-EOB-DTPA uptake capacity was relatively maintained in the secondary xenotransplanted tumors that developed in the subcutaneous lesions of the mice (Fig. 3B).

Using a retrovirus system *in vitro*, we then introduced shRNA targeting *HNF4A* (Sh-HNF4A) or scramble (Sh-Scr) into tumor cells obtained from a hyperintense HCC. We confirmed the reduction of HNF4α protein expression in Sh-HNF4A-transfected cells compared with Sh-Scr-transfected cells by western blotting (Fig. 3C, left panel). Interestingly, *HNF4A* knockdown resulted in a modest increase in *AFP* and *FOXM1* expression and a dramatic decrease in *CYP3A4* and *OATP1B3* expression (Fig. 3C, right panel). It also resulted in the loss of OATP1B3 protein expression, and striking morphological changes were confirmed by immunofluorescence and phase-contrast microscopy (Fig. 3D). Sh-HNF4A-transfected cells displayed long, thin cell shapes with neurite-like extensions, whereas Sh-Scr-transfected cells were relatively smooth and round. Sh-Scr- or Sh-HNF4A-transfected cells were further injected subcutaneously into NOD/SCID mice, and aggressive tumor growth accompanied with the loss of Gd-EOB-DTPA uptake capacity was

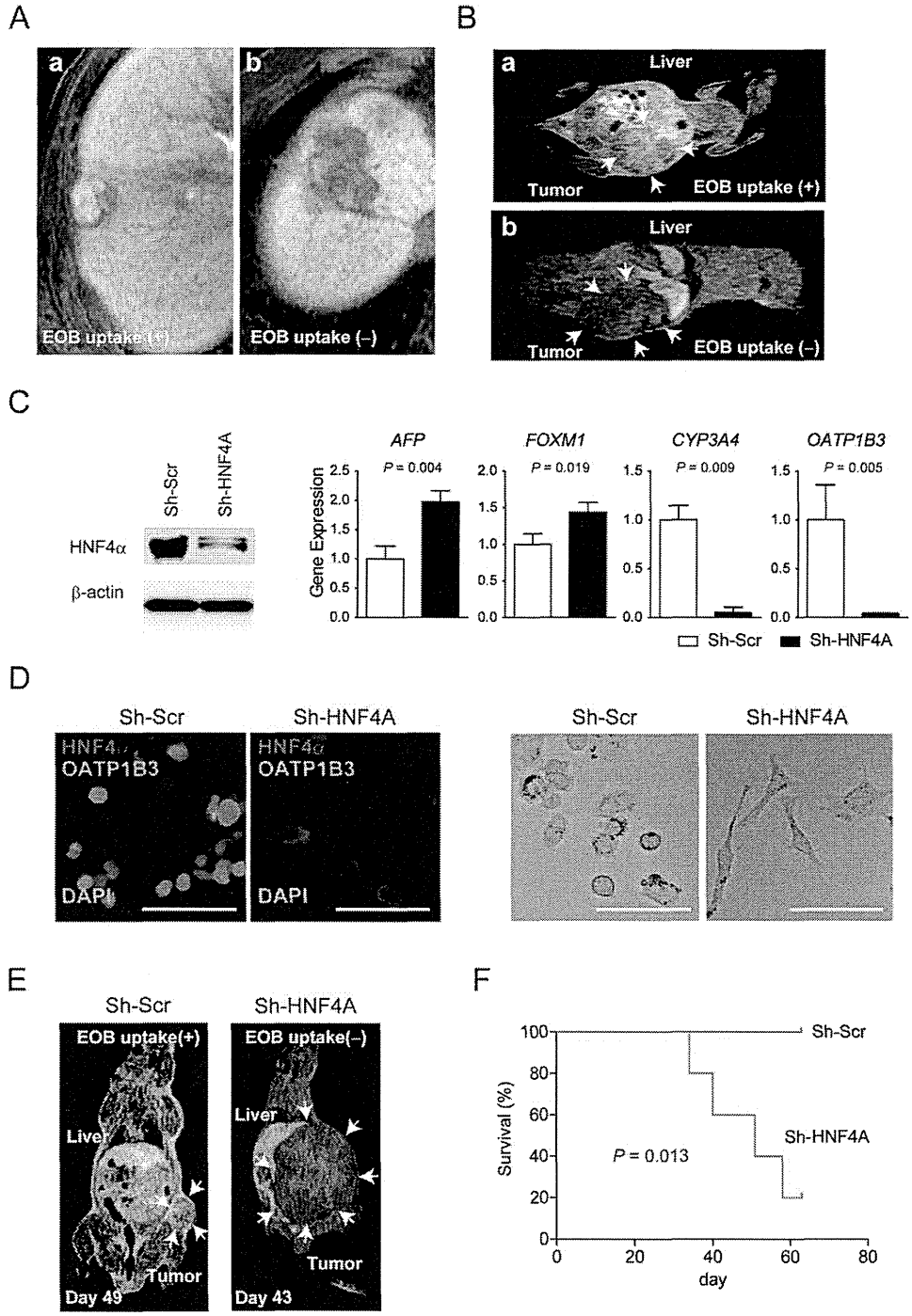

Fig. 3. HNF4α regulates a mature hepatocyte-like, less aggressive HCC phenotype coupled with Gd-EOB-DTPA uptake in hyperintense HCC. (A) MRI scans of hyperintense (a) and hypointense (b) HCCs in the hepatobiliary phase before surgery. The T/N signal intensity ratios of the images in the hepatobiliary phase were 1.02 (left panel) and 0.49 (right panel). Surgically resected specimens were subsequently used for mouse xenotransplantation. (B) MRI scans of NOD/SCID mouse xenotransplanted with hyperintense (a) and hypointense (b) HCCs in the hepatobiliary phase. The T/N signal intensity ratios of the images were 0.82 (upper panel) and 0.45 (lower panel). (C) Left panel: Expression of HNF4α protein by western blotting. Hyperintense HCC cells were harvested in dishes and treated with retroviruses encoding an expression cassette against *HNF4A* (Sh-HNF4A) or scramble sequence (Sh-Scr). Right panel: qRT-PCR of *AFP, FOXM1, CYP3A4*, and *OATP1B3* in hyperintense HCC cells transfected with Sh-Scr or Sh-HNF4A. (D) Left panel: Immunofluorescence analysis of HNF4α (red) and OATP1B3 (green) in hyperintense HCC cells transfected with Sh-Scr or Sh-HNF4A (scale bar = 100 μm). Right panel: Representative photomicrographs of hyperintense HCC cells transfected with Sh-Scr or Sh-HNF4A (scale bar = 100 μm). (E) MRI scans of NOD/SCID mouse xenotransplanted with hyperintense HCC cells transfected with Sh-Scr (day 49 after transplantation) or Sh-HNF4A (day 43 after transplantation). The T/N signal intensity ratios of the images in the hepatobiliary phase were 0.65 (left panel) and 0.34 (right panel). (F) Survival of NOD/SCID mice xenotransplanted with hyperintense HCC cells transfected with Sh-Scr (n = 5) or Sh-HNF4A (n = 5).

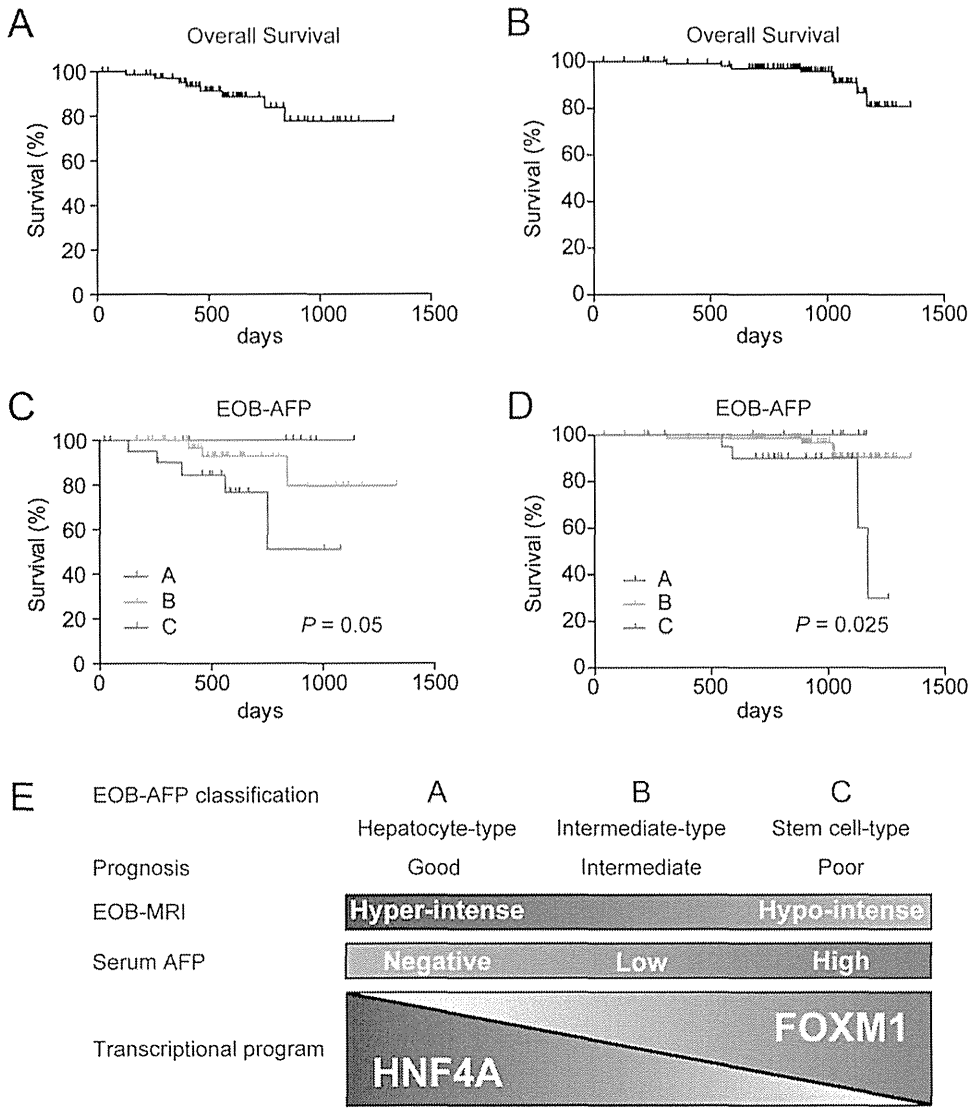

Fig. 4. Prognostic utility of the EOB-AFP classification. (A,B) Overall survival curves of Cohorts 1 (A) and 2 (B). (C,D) Overall survival curves of Cohorts 1 (C) and 2 (D) according to the EOB-AFP classification. (E) The EOB-AFP classification system and its molecular basis.

observed in Sh-HNF4A-transfected cells, whereas Sh-Scr-transfected cells still showed Gd-EOB-DTPA uptake with less tumorigenic capacity (Fig. 3E). Mice xenotransplanted with Sh-HNF4A-transfected cells had a worse prognosis compared with those xenotransplanted with Sh-Scr-transfected cells (Fig. 3F), indicating a crucial role for HNF4α in the maintenance of a mature hepatocyte-like, less aggressive HCC phenotype coupled with Gd-EOB-DTPA uptake capacity.

Prognosis of Early-Stage HCC by EOB-AFP Classification. Finally, we evaluated the prognosis of patients with HCC diagnosed by EOB-MRI and serum AFP. To exclude the potential effect of lead-time bias on survival analysis for HCCs at different stages, we evaluated the power of the EOB-AFP classification system to predict the prognosis of patients with early-stage BCLC stage 0 or A HCCs diagnosed by EOB-MRI in an independent multicenter cohort (Cohort 2). Nine of the 109 HCC cases (8.3%) were diagnosed with hyperintense HCCs and were found to be significantly associated with low serum AFP levels (Table 1). The clinicopathologic characteristics of the patients defined by the EOB-AFP classification are shown in Supporting Table 5. The median follow-up times in Cohorts 1 and 2 were 569 and 932 days, respectively. The 3-year overall survival rates in Cohorts 1 and 2 were 77.7% and 90.9%, respectively (Fig. 4A,B). The prognosis of HCC patients was not separated by TNM or BCLC stages because most of these patients were diagnosed at early stages (Fig. S4A-D); nevertheless, the EOB-AFP classification system robustly stratified HCCs according to survival with statistically significant differences between the classes (Fig. 4C,D). EOB-AFP class A patients had 100% overall survival, whereas class C patients had 30% overall survival at 1,200 days after radical resection in Cohort 2.

The prognosis of HCC patients stratified by the EOB-AFP classification was most likely affected by the malignant nature of the tumor at surgical resection, because EOB-AFP class C patients showed a 40-60% recurrence-free survival rate, whereas class A patients had a 88-100% recurrence-free survival rate at 1 year after radical resection in both cohorts (Fig. S5).

Altogether, our data, for the first time, revealed that the prognosis of early-stage HCC patients is heterogeneous and related to the malignant phenotypes of the tumors, even after successful treatment by radical resection. The EOB-AFP classification system reflects the malignant nature of the tumor and predicts the survival of early-stage HCC patients prior to surgery.

Discussion

Among several HCC staging systems currently used,[2] the BCLC system is recommended because it is linked to treatment strategy.[22] The assessment of the malignant nature of tumors coupled with current staging systems will supplement the management of early-stage HCC[23] because early recurrence after potentially curative treatment may be associated with the characteristics of the resected tumor rather than the development of a *de novo* HCC in the background liver.[24] Molecular profiling approaches have tried to evaluate the malignant features of HCCs and the surrounding noncancerous liver tissue,[3-6,12,18] although the evaluation of the potential clinical application of these approaches is ongoing. Our EOB-AFP classification system is molecularly related to the *OATP1B3* gene signature, which can be used to classify HCCs according to their stem/maturational status. Interestingly, the differential expression of *OATP1B3* was also noted in two HCC subtypes associated with the stem/maturational status, as reported recently by our group (hepatic stem cell-like and mature hepatocyte-like HCC)[12] and others (hepatoblast-type and hepatocyte type)[4] (Fig. S6). As expected, all class A HCCs were categorized as mature hepatocyte-like HCC in Cohort 1 (data not shown). The stem/maturational status defined by the EOB-AFP classification is most likely regulated by at least two transcription factors: HNF4α and FOXM1 (Fig. 4E).

HNF4α was first discovered as a liver-enriched nuclear orphan receptor activating the transcription of transthyretin genes, and it is known to regulate bile acid and cholesterol metabolism.[25] The liver-specific loss of *HNF4A* in adult mice results in hepatocyte proliferation,[26] whereas the introduction of *HNF4A* suppresses HCC growth.[27,28] Furthermore, a recent study suggested a role for *HNF4A* as a tumor suppressor in inflammation-related hepatocarcinogenesis through the regulation of microRNAs.[29] The present study demonstrated a crucial role for HNF4α in maintaining a hepatocyte-like, less aggressive phenotype coupled with Gd-EOB-DTPA uptake in a class A HCC by directly modifying *HNF4A* gene expression. Thus, *HNF4A* may work as a tumor suppressor gene and inhibit the progression of HCC, which may be related to the good prognosis of class A HCCs.

FOXM1 belongs to the forkhead superfamily of transcription factors and regulates a myriad of biologic processes including cell proliferation and differentiation.[30] The pivotal role of FOXM1 in liver development and regeneration has been reported previously.[17] FOXM1 was also required for HCC development in a mouse hepatocarcinogenesis model[31] and acted as an oncogene in a transgenic mouse model.[32] It was recently shown that FOXM1 levels are elevated in various cancers including HCC.[32,33] A prognostic role for FOXM1 in HCC patients after liver transplantation was also reported[34]; this may be associated with the metastatic capacity of tumors regulated by FOXM1.[35] As FOXM1 and AFP are known to be activated during liver regeneration and hepatocarcinogenesis, serum AFP levels may be a surrogate marker for the expression status of FOXM1 and thus facilitate the prognostic stratification of HCCs by the EOB-AFP classification.

Among the molecular markers reported to be differentially expressed between dysplastic nodule and well-differentiated HCC, we found preferential overexpression of GS in EOB-AFP class A and GPC-3 in class C HCCs. Our data suggest that class A and class C HCCs may follow different processes of early hepatocarcinogenesis events that might be associated with the differential activation of HNF4α and FOXM1, and further studies are required to obtain molecular insights into these processes.

Our overall survival data in Cohort 2 indicated that EOB-AFP class A patients had 100% overall survival, whereas class C patients had 30% overall survival at 1,200 days after radical resection. This suggests that the micro-dissemination of tumor cells in EOB-AFP class C HCC patients has already occurred by the time they are diagnosed with early-stage disease. Indeed, 50% of all class C patients showed tumor recurrence, whereas 88-100% of class A patients showed no recurrence within 1 year of resection; this is consistent with a recent study evaluating the clinical features of hyperintense HCCs[36] and may be due to

the overexpression of FOXM1, which results in the activation of metastatic programs. Therefore, these patients might have survival benefits if they receive adjuvant therapies. As several adjuvant therapies might be beneficial for HCC patients after surgical resection,[37] integration of the EOB-AFP classification system into current staging practices may provide additional therapeutic options for early-stage HCC patients who will receive surgery.

A limitation of the present study is that we used three different cohorts to reveal the molecular portraits associated with clinical imaging and prognosis (i.e., the microarray cohort of 238 HCCs of various stages for the evaluation of molecular profiling; Cohort 1 for the validation of molecular profiling and EOB-MRI findings in various stages of HCC; and Cohort 2 for evaluating the utility of EOB-MRI and serum AFP in predicting the prognosis of early-stage HCCs), which made the molecular and prognostic analyses complex. Another limitation of this study was in the evaluation of prognostic utility because it uses small retrospective cohorts. Direct evaluation of the molecular profiles and prognostic values of hyperintense HCCs should be performed in a prospective study using a large-scale HCC cohort.

Taken together, the present study demonstrates for the first time that the combined approach of noninvasive Gd-EOB-DTPA-enhanced MRI and serum AFP levels can be used preoperatively to classify resectable HCCs into three subgroups with distinct prognoses. This classification is molecularly related to the stem/maturation status of HCCs regulated by HNF4α and FOXM1. The multicenter early-stage HCC cohort that received radical resection revealed that the EOB-AFP classification is clinically useful to determine the prognosis of early-stage HCC patients. On the basis of these observations, we propose that the EOB-AFP classification system be incorporated into current HCC staging practices, especially for the management of early-stage HCCs.

Acknowledgment: We thank Drs. Yutaka Aoyagi (Division of Gastroenterology and Hepatology, Niigata University Graduate School of Medical and Dental Sciences, Niigata, Japan), Hiroko Iijima (Division of Hepatobiliary and Pancreatic Disease, Department of Internal Medicine, Hyogo College of Medicine, Hyogo, Japan), and Michio Sata (Division of Gastroenterology, Department of Medicine, Kurume University School of Medicine, Kurume, Japan) for help with patient enrollment. We also thank Mss. Masayo Baba and Nami Nishiyama for excellent technical assistance.

References

1. Jemal A, Bray F, Center MM, Ferlay J, Ward E, Forman D. Global cancer statistics. CA Cancer J Clin 2011;61:69-90.
2. Sala M, Forner A, Varela M, Bruix J. Prognostic prediction in patients with hepatocellular carcinoma. Semin Liver Dis 2005;25:171-180.
3. Cairo S, Wang Y, de Reynies A, Duroure K, Dahan J, Redon MJ, et al. Stem cell-like micro-RNA signature driven by Myc in aggressive liver cancer. Proc Natl Acad Sci U S A 2010;107:20471-20476.
4. Lee JS, Heo J, Libbrecht L, Chu IS, Kaposi-Novak P, Calvisi DF, et al. A novel prognostic subtype of human hepatocellular carcinoma derived from hepatic progenitor cells. Nat Med 2006;12:410-416.
5. Marquardt JU, Raggi C, Andersen JB, Seo D, Avital I, Geller D, et al. Human hepatic cancer stem cells are characterized by common stemness traits and diverse oncogenic pathways. HEPATOLOGY 2011;54:1031-1042.
6. Yamashita T, Ji J, Budhu A, Forgues M, Yang W, Wang HY, et al. EpCAM-positive hepatocellular carcinoma cells are tumor-initiating cells with stem/progenitor cell features. Gastroenterology 2009;136:1012-1024.
7. Yamashita T, Wang XW. Cancer stem cells in the development of liver cancer. J Clin Invest 2013;123:1911-1918.
8. Reimer P, Schneider G, Schima W. Hepatobiliary contrast agents for contrast-enhanced MRI of the liver: properties, clinical development and applications. Eur Radiol 2004;14:559-578.
9. Kanki A, Tamada T, Higaki A, Noda Y, Tanimoto D, Sato T, et al. Hepatic parenchymal enhancement at Gd-EOB-DTPA-enhanced MR imaging: correlation with morphological grading of severity in cirrhosis and chronic hepatitis. Magn Reson Imaging 2012;30:356-360.
10. Kitao A, Matsui O, Yoneda N, Kozaka K, Shinmura R, Koda W, et al. The uptake transporter OATP8 expression decreases during multistep hepatocarcinogenesis: correlation with gadoxetic acid enhanced MR imaging. Eur Radiol 2011;21:2056-2066.
11. Kitao A, Zen Y, Matsui O, Gabata T, Kobayashi S, Koda W, et al. Hepatocellular carcinoma: signal intensity at gadoxetic acid-enhanced MR Imaging—correlation with molecular transporters and histopathologic features. Radiology 2010;256:817-826.
12. Yamashita T, Forgues M, Wang W, Kim JW, Ye Q, Jia H, et al. EpCAM and alpha-fetoprotein expression defines novel prognostic subtypes of hepatocellular carcinoma. Cancer Res 2008;68:1451-1461.
13. Yamashita T, Honda M, Nakamoto Y, Baba M, Nio K, Hara Y, et al. Discrete nature of EpCAM(+) and CD90(+) cancer stem cells in human hepatocellular carcinoma. HEPATOLOGY 2013;57:1484-1497.
14. Yamashita T, Honda M, Nio K, Nakamoto Y, Takamura H, Tani T, et al. Oncostatin m renders epithelial cell adhesion molecule-positive liver cancer stem cells sensitive to 5-Fluorouracil by inducing hepatocytic differentiation. Cancer Res 2010;70:4687-4697.
15. Lade AG, Monga SP. Beta-catenin signaling in hepatic development and progenitors: which way does the WNT blow? Dev Dyn 2011;240:486-500.
16. Trauner M, Halilbasic E. Nuclear receptors as new perspective for the management of liver diseases. Gastroenterology 2011;140:1120-1125 e1121-1112.
17. Wang X, Kiyokawa H, Dennewitz MB, Costa RH. The Forkhead Box m1b transcription factor is essential for hepatocyte DNA replication and mitosis during mouse liver regeneration. Proc Natl Acad Sci U S A 2002;99:16881-16886.
18. Hoshida Y, Villanueva A, Kobayashi M, Peix J, Chiang DY, Camargo A, et al. Gene expression in fixed tissues and outcome in hepatocellular carcinoma. N Engl J Med 2008;359:1995-2004.
19. Ji J, Shi J, Budhu A, Yu Z, Forgues M, Roessler S, et al. MicroRNA expression, survival, and response to interferon in liver cancer. N Engl J Med 2009;361:1437-1447.
20. Di Tommaso L, Destro A, Seok JY, Balladore E, Terracciano L, Sangiovanni A, et al. The application of markers (HSP70 GPC3 and GS) in liver biopsies is useful for detection of hepatocellular carcinoma. J Hepatol 2009;50:746-754.

21. Llovet JM, Chen Y, Wurmbach E, Roayaie S, Fiel MI, Schwartz M, et al. A molecular signature to discriminate dysplastic nodules from early hepatocellular carcinoma in HCV cirrhosis. Gastroenterology 2006;131:1758-1767.
22. Sherman M. Hepatocellular carcinoma: screening and staging. Clin Liver Dis 2011;15:323-334, vii-x.
23. Villanueva A, Hoshida Y, Toffanin S, Lachenmayer A, Alsinet C, Savic R, et al. New strategies in hepatocellular carcinoma: genomic prognostic markers. Clin Cancer Res 2010;16:4688-4694.
24. de Lope CR, Tremosini S, Forner A, Reig M, Bruix J. Management of HCC. J Hepatol 2012;56 Suppl:S75-87.
25. Crestani M, De Fabiani E, Caruso D, Mitro N, Gilardi F, Vigil Chacon AB, et al. LXR (liver X receptor) and HNF-4 (hepatocyte nuclear factor-4): key regulators in reverse cholesterol transport. Biochem Soc Trans 2004;32:92-96.
26. Bonzo JA, Ferry CH, Matsubara T, Kim JH, Gonzalez FJ. Suppression of hepatocyte proliferation by hepatocyte nuclear factor 4alpha in adult mice. J Biol Chem 2012;287:7345-7356.
27. Ning BF, Ding J, Yin C, Zhong W, Wu K, Zeng X, et al. Hepatocyte nuclear factor 4 alpha suppresses the development of hepatocellular carcinoma. Cancer Res 2010;70:7640-7651.
28. Yin C, Lin Y, Zhang X, Chen YX, Zeng X, Yue HY, et al. Differentiation therapy of hepatocellular carcinoma in mice with recombinant adenovirus carrying hepatocyte nuclear factor-4alpha gene. HEPATOLOGY 2008;48:1528-1539.
29. Hatziapostolou M, Polytarchou C, Aggelidou E, Drakaki A, Poultsides GA, Jaeger SA, et al. An HNF4alpha-miRNA inflammatory feedback circuit regulates hepatocellular oncogenesis. Cell 2011;147:1233-1247.
30. Koo CY, Muir KW, Lam EW. FOXM1: From cancer initiation to progression and treatment. Biochim Biophys Acta 2012;1819:28-37.
31. Kalinichenko VV, Major ML, Wang X, Petrovic V, Kuechle J, Yoder HM, et al. Foxm1b transcription factor is essential for development of hepatocellular carcinomas and is negatively regulated by the p19ARF tumor suppressor. Genes Dev 2004;18:830-850.
32. Kalin TV, Ustiyan V, Kalinichenko VV. Multiple faces of FoxM1 transcription factor: lessons from transgenic mouse models. Cell Cycle 2011;10:396-405.
33. Calvisi DF, Pinna F, Ladu S, Pellegrino R, Simile MM, Frau M, et al. Forkhead box M1B is a determinant of rat susceptibility to hepatocarcinogenesis and sustains ERK activity in human HCC. Gut 2009;58:679-687.
34. Sun H, Teng M, Liu J, Jin D, Wu J, Yan D, et al. FOXM1 expression predicts the prognosis in hepatocellular carcinoma patients after orthotopic liver transplantation combined with the Milan criteria. Cancer Lett 2011;306:214-222.
35. Raychaudhuri P, Park HJ. FoxM1: a master regulator of tumor metastasis. Cancer Res 2011;71:4329-4333.
36. Kitao A, Matsui O, Yoneda N, Kozaka K, Kobayashi S, Koda W, et al. Hypervascular hepatocellular carcinoma: correlation between biologic features and signal intensity on gadoxetic acid-enhanced MR images. Radiology 2012;265:780-789.
37. Zhong JF, Li H, Li LQ, You XM, Zhang Y, Zhao YN, et al. Adjuvant therapy options following curative treatment of hepatocellular carcinoma: a systematic review of randomized trials. Eur J Surg Oncol 2012;38:286-295.

Supporting Information

Additional Supporting Information may be found in the online version of this article at the publisher's website.

Diabetologia (2014) 57:1968–1976
DOI 10.1007/s00125-014-3306-9

ARTICLE

Selenoprotein P as a diabetes-associated hepatokine that impairs angiogenesis by inducing VEGF resistance in vascular endothelial cells

Kazuhide Ishikura · Hirofumi Misu · Masafumi Kumazaki · Hiroaki Takayama · Naoto Matsuzawa-Nagata · Natsumi Tajima · Keita Chikamoto · Fei Lan · Hitoshi Ando · Tsuguhito Ota · Masaru Sakurai · Yumie Takeshita · Kenichiro Kato · Akio Fujimura · Ken-ichi Miyamoto · Yoshiro Saito · Satomi Kameo · Yasuo Okamoto · Yoh Takuwa · Kazuhiko Takahashi · Hiroyasu Kidoya · Nobuyuki Takakura · Shuichi Kaneko · Toshinari Takamura

Received: 10 January 2014 / Accepted: 30 May 2014 / Published online: 3 July 2014

Abstract

Aims/hypothesis Impaired angiogenesis induced by vascular endothelial growth factor (VEGF) resistance is a hallmark of vascular complications in type 2 diabetes; however, its molecular mechanism is not fully understood. We have previously identified selenoprotein P (SeP, encoded by the *SEPP1* gene in humans) as a liver-derived secretory protein that induces insulin resistance. Levels of serum SeP and hepatic expression of *SEPP1* are elevated in type 2 diabetes. Here, we investigated the effects of SeP on VEGF signalling and angiogenesis.

Methods We assessed the action of glucose on *Sepp1* expression in cultured hepatocytes. We examined the actions of SeP on VEGF signalling and VEGF-induced angiogenesis in HUVECs. We assessed wound healing in mice with hepatic SeP overexpression or SeP deletion. The blood flow recovery after ischaemia was also examined by using hindlimb ischaemia model with *Sepp1*-heterozygous-knockout mice.

Kazuhide Ishikura, Hirofumi Misu and Masafumi Kumazaki contributed equally to this work.

Electronic supplementary material The online version of this article (doi:10.1007/s00125-014-3306-9) contains peer-reviewed but unedited supplementary material, which is available to authorised users.

K. Ishikura · H. Misu · M. Kumazaki · H. Takayama · N. Matsuzawa-Nagata · N. Tajima · K. Chikamoto · F. Lan · H. Ando · T. Ota · M. Sakurai · Y. Takeshita · K. Kato · S. Kaneko · T. Takamura (✉)
Department of Disease Control and Homeostasis, Kanazawa University Graduate School of Medical Sciences, 13-1 Takara-machi, Kanazawa, Ishikawa 920-8641, Japan
e-mail: ttakamura@m-kanazawa.jp

M. Kumazaki · H. Ando · A. Fujimura
Division of Clinical Pharmacology, Department of Pharmacology, Jichi Medical University, Tochigi, Japan

N. Matsuzawa-Nagata · K. Miyamoto
Department of Medicinal Informatics, Kanazawa University Graduate School of Medical Sciences, Kanazawa, Ishikawa, Japan

M. Sakurai
Department of Epidemiology and Public Health, Kanazawa Medical University, Uchinada, Japan

Y. Saito
Department of Medical Life Systems, Faculty of Medical and Life Sciences, Doshisha University, Kyotanabe, Kyoto, Japan

S. Kameo
Department of Public Health, Gunma University Graduate School of Medicine, Gunma, Japan

Y. Okamoto · Y. Takuwa
Department of Physiology, Kanazawa University Graduate School of Medical Sciences, Kanazawa, Ishikawa, Japan

K. Takahashi
Department of Nutritional Biochemistry, Hokkaido Pharmaceutical University, Otaru, Hokkaido, Japan

H. Kidoya · N. Takakura
Department of Signal Transduction, Research Institute for Microbial Diseases, Osaka University, Osaka, Japan

Results Treatment with glucose increased gene expression and transcriptional activity for *Sepp1* in H4IIEC hepatocytes. Physiological concentrations of SeP inhibited VEGF-stimulated cell proliferation, tubule formation and migration in HUVECs. SeP suppressed VEGF-induced reactive oxygen species (ROS) generation and phosphorylation of VEGF receptor 2 (VEGFR2) and extracellular signal-regulated kinase 1/2 (ERK1/2) in HUVECs. Wound closure was impaired in the mice overexpressing *Sepp1*, whereas it was improved in $SeP^{-/-}$mice. $SeP^{+/-}$mice showed an increase in blood flow recovery and vascular endothelial cells after hindlimb ischaemia.

Conclusions/interpretation The hepatokine SeP may be a novel therapeutic target for impaired angiogenesis in type 2 diabetes.

Keywords Angiogenesis · Hepatokine · ROS · Selenoprotein P · VEGF

Abbreviations

BSO	Buthionine sulfoximine
DCF	2′,7′-Dichlorofluorescein diacetate
ERK1/2	Extracellular signal-regulated kinase 1/2
MAPK	Mitogen-activated protein kinase
ROS	Reactive oxygen species
SeP	Selenoprotein P
VEGF(R)	Vascular endothelial growth factor (receptor)

Introduction

Type 2 diabetes is a chronic hyperglycaemic condition that causes various vascular complications, including damage to: small blood vessels, resulting in retinopathy, nephropathy and neuropathy; and large blood vessels, resulting in cardiovascular diseases. Earlier improved glycaemic control is associated with reduced risk for cardiovascular disease in people with type 2 diabetes [1]. However, more recent clinical trials have indicated that strict glycaemic control does not necessarily prevent vascular complications [2]. Hence, beyond glycaemic control, novel therapies to directly treat vascular disease are needed to improve the prognosis of people with type 2 diabetes.

Angiogenesis is a physiological process involving the growth of new blood vessels from pre-existing vascular structures and the subsequent formation of a vascular network. A number of abnormalities associated with angiogenesis have been observed in people with type 2 diabetes [3], and impaired angiogenesis is linked to the development of various vascular complications in diabetes mellitus. Compared with control individuals without diabetes, people with type 2 diabetes show poor development of coronary collateral vessels on coronary angiography [4]. Moreover, a previous study using autopsied hearts reported that people with diabetes have significantly lower capillary densities in areas of myocardial infarction [5]. These reports suggest that the angiogenic response to infarction and/or ischaemia is inhibited at the levels of capillaries and small arterioles in type 2 diabetes. Inadequate vascular formation could attenuate perfusion recovery in response to ischaemia, thereby partially accounting for the poor clinical outcomes in type 2 diabetic patients with coronary heart disease or peripheral artery disease [6, 7]. In addition, insufficient angiogenesis is involved in abnormal wound healing and the development of diabetic skin ulcers [8].

Vascular endothelial growth factor (VEGF) is a major mediator of angiogenesis under physiological and pathophysiological conditions. VEGF binds and phosphorylates its receptors, leading to the activation of a variety of signalling cascades such as the mitogen-activated protein kinase (MAPK) and Akt cascades. Angiogenic gene therapy using plasmids encoding VEGF has been attempted in patients with coronary or peripheral artery diseases [9]. However, diabetes mellitus people often show a poor response to therapeutic angiogenesis [10]. Therefore, VEGF resistance, a defect of VEGF-related signal transduction, has been postulated as a molecular basis for the dysregulated angiogenesis in diabetes mellitus [3, 11]. The molecular mechanisms underlying VEGF resistance in diabetes mellitus are not fully understood.

Selenoprotein P (SeP, encoded by *SEPP1* in humans and *Sepp1* in mice) is a secretory protein produced primarily in the liver [12, 13]. It contains ten selenocysteine residues and functions as a selenium supply protein [14]. We have previously reported that levels of serum SeP and hepatic gene expression of *SEPP1* are elevated in type 2 diabetes [15]. More recently, Yang et al have reported that serum levels of SeP are increased in people with impaired glucose tolerance [16]. SeP impairs insulin signal transduction and induces dysregulation of glucose metabolism in skeletal muscle and liver, indicating that SeP functions as a type 2 diabetes-associated hepatokine that causes insulin resistance and hyperglycaemia [15]. SeP has heparin-binding properties [17] and is associated with endothelial cells in rat tissues [18], suggesting that SeP exerts some actions on vascular endothelial cells. A previous study using in vitro techniques reported that SeP has an antioxidative action in vascular endothelial cells [19]. Nevertheless, it is unknown whether SeP plays a role in the angiogenic response.

We speculated that the liver-derived secretory protein SeP contributes to angiogenesis-associated vascular complications in type 2 diabetes by acting directly on vascular endothelial cells. In the current study, we investigated the effects of SeP on angiogenesis in normal conditions, independently of diabetes, using purified SeP protein and *Sepp1*-deficient mice without the induction of diabetes.

Methods

Cell culture HUVECs were cultured in HuMedia EG2 (Kurabo, Osaka, Japan). H4-II-E-C3 cells were cultured in 10% (vol./vol.) fetal bovine serum (FBS)/DMEM (Gibco, Carlsbad, CA, USA) as previously described [20]. All cellular experiments were approved by the Committee for Cellular Study at our Institute.

Animals The *Sepp1*-deleted mice were produced by homologous recombination with genomic DNA cloned from a Sv-129 P1 library [21]. All animal studies were approved by the Committee for Animal Studies at our Institute. See the electronic supplementary material (ESM) for further details.

Measurement of selenium Total selenium concentrations were determined using a modification of Watkinson's method [22, 23]. See the ESM for further details.

SEPP1 promoter assay The human *SEPP1* promoter region was cloned to a luciferase reporter vector, and luciferase activities were measured using the dual luciferase assay system (Promega, Madison, WI, USA) [20]. See the ESM for further details.

Cell proliferation assay HUVECs were quantified using Cell Counting Kit-8 (Wako, Osaka, Japan). See the ESM for further details.

Migration assay HUVECs were seeded in the upper chamber of polycarbonate filters, and the number of cells migrating across the filter was counted. See the ESM for further details.

Cell tubule formation assay HUVECs were seeded on plates coated with ECMatrix gel. Endothelial tubule formation was photographed under a microscope. See the ESM for further details.

Matrigel plug implantation assay This assay was performed using a directed in vivo angiogenesis assay inhibition kit (Trevigen, Gaithersburg, MD, USA). See the ESM for further details.

Western blot analysis HUVECs were pretreated with SeP for 24 h. After 2 h of starvation, HUVECs were stimulated with VEGF for 15 min. See the ESM for further details.

RNA preparation and quantitative real-time Real-time PCR was performed on an ABI-Prism 7900HT (Applied Biosystems, Carlsbad, CA, USA). See the ESM for further details.

Reactive oxygen species generation Intracellular reactive oxygen species (ROS) levels were measured using 2′,7′-dichlorofluorescein diacetate (DCF) and quantified using a fluorescent plate reader (Fluoroskan Ascent FL, Yokohama, Japan). See the ESM for further details.

Purification of SeP SeP was purified from human plasma using conventional chromatographic methods [14, 24]. See the ESM for further details.

Preparation of human SEPP1 plasmids and overexpression of SeP in mice The human *SEPP1* expression plasmids were provided by Kaketsuken (The Chemo-Sero-Therapeutic Research Institute, Tokyo, Japan). Plasmid was injected into the tail vein of mice. See the ESM for further details.

Measurement of serum human SeP in mice injected with human SEPP1 plasmid Serum levels of human SeP were measured by enzyme-linked immunosorbent assays using two monoclonal antibodies [15, 25].

Mouse wound healing model Full-thickness wound was created, and the extent of wound closure was examined. See the ESM for further details.

Hindlimb ischaemia model Mice underwent ligation and segmental resection of the left femoral vessel [26]. See the ESM for further details.

Identification of $CD31^+$ vessels An antibody to CD31 was used for immunostaining. See the ESM for further details.

Calculations and statistical analysis All data were analysed using SPSS version 11.0 (Japanese Windows Edition; SPSS, www.ibm.com/software/analytics/spss/). See the ESM for further details.

Results

Glucose increases gene expression and transcriptional activity for SeP in cultured hepatocytes To confirm the elevation of SeP in the livers of people and animal models with type 2 diabetes [15], we examined the action of glucose on *Sepp1* expression in H4-II-EC hepatocytes (Fig. 1). *Sepp1* mRNA expression was significantly increased by 25 mmol/l glucose in a time-dependent manner (Fig. 1a). Additionally, *SEPP1* promoter activity as measured by luciferase activity was increased by 25 mmol/l glucose compared with mannitol (Fig. 1b). These results are consistent with our previous findings showing that treatment with high glucose increases protein levels of SeP in mouse primary hepatocytes [15]. These results indicate that high concentrations of glucose increase the transcriptional activity of SeP genes in the cultured hepatocytes.

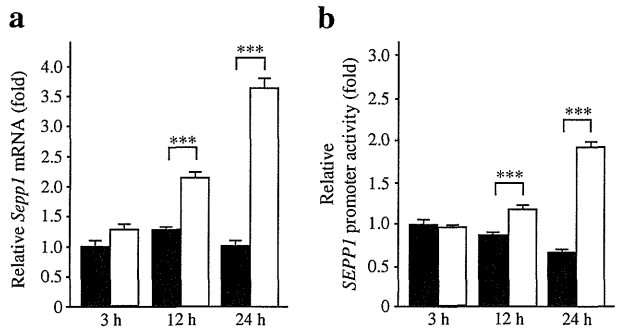

Fig. 1 Glucose increases gene expression and transcriptional activity for SeP in H4-II-EC3 hepatocytes. (**a**) Relative *Sepp1* mRNA expression normalised to β-actin. (**b**) Promoter activity for *SEPP1* in H4-II-EC3 hepatocytes treated with glucose and mannitol. Data are mean ± SD, $n=3$, ***$p<0.001$. White bars, glucose; black bars, mannitol

SeP impairs VEGF-induced angiogenesis in endothelial cells To assess the direct action of the liver-derived secretory protein SeP on vascular endothelial cells, we treated HUVECs with purified human SeP protein. HUVECs were treated with 5 or 10 μg/ml purified human SeP protein, corresponding to serum levels of SeP in healthy individuals or people with type 2 diabetes [15]. In addition, we confirmed that levels of selenium were undetectable (less than 2.5 ng/ml) in all the culture media used for HUVECs. VEGF-induced proliferation of HUVECs was significantly suppressed by treatment with 10 μg/ml SeP (Fig. 2a). Co-administration of buthionine sulfoximine (BSO), an inhibitor of glutathione synthesis, partly rescued the suppressive effect of SeP.

Next, we examined the effects of SeP on VEGF-induced migration in HUVECs. VEGF promoted the migration of HUVECs across polycarbonate filters. This migration was inhibited by the addition of SeP in a concentration-dependent manner (Fig. 2b, c). In the absence of VEGF, treatment with SeP did not affect the migration of HUVECs, suggesting that SeP modulates VEGF-dependent migration of endothelial cells. We further examined the effects of SeP on tubule formation in HUVECs. HUVECs cultured on Matrigel containing VEGF showed morphological tubule formation, with a lumen surrounded by endothelial cells adhering to one another (Fig. 2d). SeP inhibited tubule formation of HUVECs in a concentration-dependent manner (Fig. 2d–e). These in vitro results indicate that SeP at physiological concentrations impairs VEGF-dependent angiogenesis of vascular endothelial cells.

SeP reduces VEGF-stimulated formation of new vessels in Matrigel The role of SeP in angiogenesis in vivo was further determined by Matrigel plug implantation assay. Matrigel was mixed with VEGF in the presence or absence of SeP protein and the plugs were implanted into the dorsal subcutaneous tissue of mice. After 10 days, angiogenesis inside the Matrigel was quantified. SeP markedly inhibited VEGF-stimulated

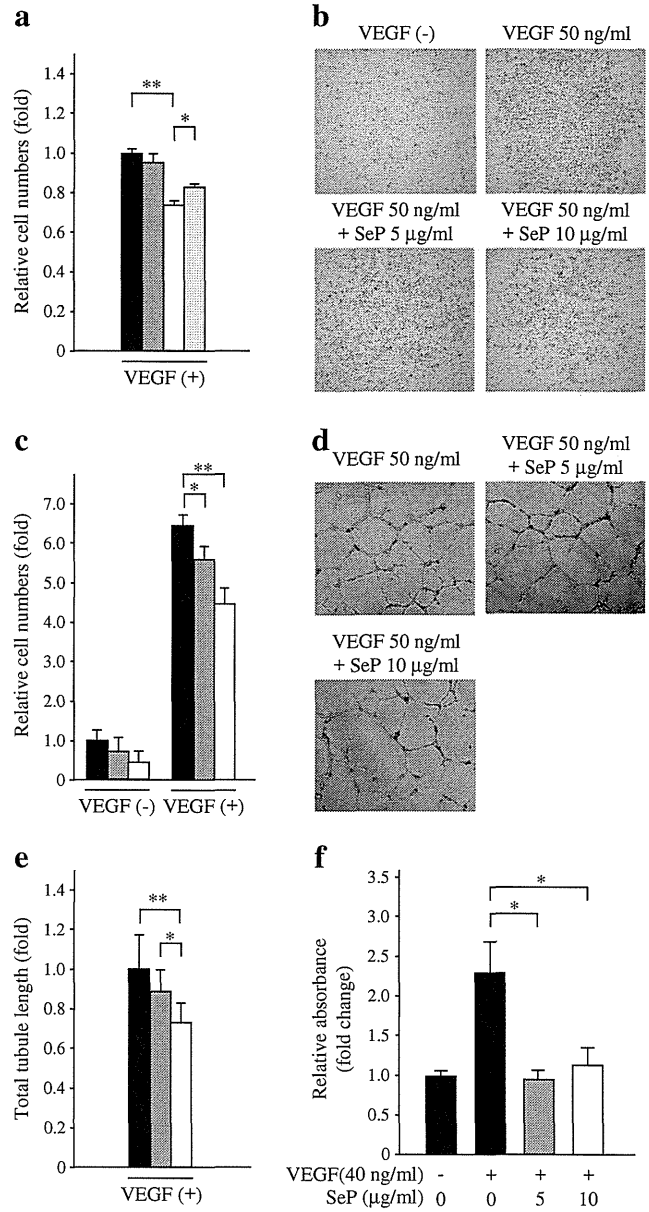

Fig. 2 SeP suppresses VEGF-stimulated angiogenesis in vascular endothelial cells. (**a**) Cell proliferation in HUVECs treated with VEGF for 48 h ($n=12$). (**b**) Representative images of HUVECs that migrated across the polycarbonate filters (magnification×200). (**c**) Quantification of HUVECs that migrated across the filters ($n=8$). (**d**) Representative images of HUVECs that were subjected to Matrigel tubule formation assay (magnification×400). (**e**) Quantification of total tubule length of HUVECs ($n=9$). (**f**) Matrigel implant assay in mice ($n=6$–8). Data are mean ± SEM, *$p<0.05$ and **$p<0.01$. Black bars, control; dark-grey bars, SeP 5 μg/ml; white bars, SeP 10 μg/ml; light-grey bars, SeP 10 μg/ml and BSO 0.2 mmol/l

formation of new vessels in the Matrigel (Fig. 2f). These results further indicate that SeP impairs angiogenesis in vivo.

SeP impairs VEGF signal transduction in endothelial cells Next, we determined whether SeP affects VEGF signal transduction in endothelial cells. Pretreatment with SeP